Micromechanical modeling
of microcracked brittle solids

M. Basista and W. Węglewski

Institute of Fundamental Technological Research,
Polish Academy of Sciences,
Świętokrzyska 21, 00-049 Warszawa, Poland
mbasista@ippt.gov.pl

The series of lectures is centered on application of micromechanics to describe nonlinear response of rock-like solids (rocks, concrete, ceramics) subject to mechanical loading and/or aggressive environmental agents. Firstly, microcrack models of brittle deformation under quasi-static loading conditions are presented. Starting with basic mechanisms of microcrack growth under tension and compression, nonlinear stress-strain relationships are derived within the Rice thermodynamic framework with microstructural internal variables. Specifically, expressions for the Gibbs complementary energy are computed using micromechanical analyses from which the micromechanical fluxes and the conjugated thermodynamic forces are identified. The kinetic equations for the microstructural internal variables are obtained. Making use of the Rice (1971) fundamental micro-to-macro transition relation, nonlinear macroscopic incremental constitutive equations are derived and confronted with test data. Microcrack interaction effects are accounted for using the method of Kachanov (1987) extended to account for cohesive-frictional resistance on crack faces in compressive stress fields. Secondly, a chemo-micromechanical model of environmental damage in concrete due to chemically aggressive ambient is presented. In particular, this model deals with deformation of hardened concrete exposed to chemical corrosion by sulfate ions migrating from the ground water through the pore network of a concrete structure. The model involves several coupled physico-chemical processes such as nonsteady diffusion, heterogeneous chemical reactions, expansion of reaction products, microcracking of heterogeneous matrix (hardened cement paste with *ettringite* inclusions) and percolation. These processes are modeled on the microscale and the resulting equations are volume-averaged leading to macroscopic expansions which closely match the test data on ASTM recommended specimens. Thirdly, the advantages and deficiencies of lattice modeling applied to microcracked brittle materials are discussed.

Key words: *brittle deformation, microcracking, crack interaction, chemo-damage, lattice models*

Preliminaries

The deformation of rocks, concrete and ceramics (collectively *rock-like* materials) under quasi-static mechanical loading has a number of features in common which result from the intrinsic heterogeneous microstructure of these materials. For example, the nonlinear behavior reported from tension or compression tests is, according to numerous literature sources, to be traced back to the internal microcracking (damage) rather than plastic deformation provided that brittle-ductile transition has not taken place. Typical failure modes observed in this class of materials are splitting and shear banding. A particular failure mode strongly depends on the amount and sign of the lateral pressure as well as end-boundary conditions.

The tensile damage in polycrystalline rocks loaded in displacement-controlled tests consists in gradual activation of the most favorably oriented and largest preexisting microcracks located at the grain boundaries or within the grains of inferior strength. A destabilized microcrack grows unstably until it is forced to stop by the superior toughness of an adjacent grain. As the external load is further increased, more and more preexisting microcracks become activated causing nonlinear overall rock response. The tensile fracture of a brittle rock is relatively simple and thoroughly understood. At a certain load level, one of the previously activated and arrested microcracks becomes critical again as the K_I at its tip exceeds locally the fracture toughness K_{Ic} of the surrounding material. In all probability, the rock inhomogeneity is unable to trap the crack again for the much longer crack sees the surrounding material as nearly homogeneous. The final rupture may thus be seen as an unstable growth of a single macroscopic crack.

When exposed to compressive loading, polycrystalline rocks exhibit a very complex nonlinear response. The following effects are usually observed in confined and unconfined compression tests (cf. [16, 47, 86, 118]): threshold-type deviation from linear elastic behavior, gradual degradation of elastic constants, influence of confining pressure on ultimate strength and failure

modes, positive dilatancy (nonlinear volume increase), anisotropy induced by directional process of microcrack evolution, hysteresis loops in stress-strain curves in loading-unloading-reloading cycles, pronounced permanent volumetric strain after complete unloading, softening regime in strain-controlled tests. Most of these features are intimately related to material damage and fracture processes accompanying rock deformation. Generally speaking, the compressive damage in rocks is much more complex than the tensile one since it is not just instability of a single most favorably oriented crack but a cooperative action of a distributed microcrack array. The cooperative damage process by which these microcracks produce the macroscopic failure has remained one of the most elusive problems of modern fracture mechanics. There is no doubt, however, that final failure occurs at a stress which can be much larger than the one at which individual microcracks become active. Hence microcrack interactions must play a vital role in compressive fracture of rocks. The confining (compressive) stress plays a stabilizing role in the microcrack growth. If there is no confinement, the final failure is typically unstable and is brought about by the propagation of a few axial cracks forming a vertical splitting surface. By contrast, even a small amount of lateral compressive stress makes individual microcracks extend in a stable manner. A microcrack will extend once the fracture toughness K_{Ic} is exceeded locally to relieve the local stress concentrations, and will then arrest. However, under compression the stress intensity factor is a decreasing function of the microcrack length and individual microcracks only extend until equilibrium $K_I = K_{Ic}$ is reached. An increase in stress difference is needed for further growth of the arrested microcracks and to activate other as yet dormant microcracks. Once the microcrack has grown relaxing the stress locally in a high stress zone, it becomes a relatively low stress zone. It is very likely that the next stress relief will be accommodated by the growth of a different microcrack rather than by further extension of the same microcrack since the latter is embedded in a low stress zone. Under the conditions of increasing stress, the population of activated microcracks reaches eventually a density at which microcrack interactions start to play a crucial role. When this has happened, the simple scenario of stress relief is no more valid since the cooperative action of interacting microcracks may induce stress amplification effects on other microcracks leading ultimately to overall instability and failure. In stress-strain diagrams this situation corresponds to a flip from strain hardening to strain softening.

As for overall failure, brittle rocks in compression may fail in a bewildering variety of modes. In unconfined compression tests specimens tend to fail by vertical splitting. At low and intermediate confining pressures failure occurs by localization of deformation on a shear band (or cone fracture). At high confining pressures a single failure surface does not form but the specimen deforms in a pseudo-ductile mode (cataclastic flow) with large scale deformations and many short, homogeneously distributed microcracks. In this case, the material may flow at constant stress or manifest strain hardening.

The deformation and failure mode in rocks tested in compression are highly dependent on the end-boundary conditions. During compressive loading a frictional constraint develops at the interface between the specimen and loading device. A cylindrical geometry when placed in direct contact with rigid platens takes on a barrel shape and a nonuniform stress state develops throughout the cylinder. In material testing the occurrence of a non-uniform stress state is a serious hindrance since the observed response may then be due to unknown boundary conditions - an undesirable effect. Hence, much effort in the laboratory work goes into achievement of homogeneous deformation by finding an appropriate friction reducer, [62]. Incidentally, the compressive strength (a constant critical stress at failure), being a very useful failure parameter for ductile materials, becomes of limited utility for rock-like materials because it varies with lateral pressure, specimen size and geometry. Instead, the fracture toughness is found to be the fundamental property dictating compressive failure. This fact has long been recognized in materials science but it seems not to be the case in rock mechanics where f_c still persists despite its obvious lack of universality, [54].

The outburst of micromechanical damage models in the past two decades can, to some extent, be explained as search for remedy for the shortcomings of CDM models (cf. [56, 78, 82]). The attribute *micromechanical* is commonly attached to the class of models relating macroproperties and macroresponse of a material to its microstructure. As such, these models span two different scales, one of which is typically inhomogeneous (microscale) while the other (macroscale) is, for computational expedience, approximated by a homogeneous effective continuum. An unquestionable merit of micromechanical damage models is in their ability of explaining the physics of damage with a minimum of ambiguity and arbitrariness. The constants in a micromechanical model have clear physical interpretation. This is not to say, though, that their magnitudes can always be measured using available experimental techniques.

The response of a brittle solid in the ascending part of the stress-strain curve depends predominantly on the volume averages of defects. The effect of microcracks is felt by the material in a smoothed sense involving orientation-weighed volume averages of microcracks. Consequently, the pre-peak response can accurately be represented using micromechanical models based on the representative volume element (RVE) and the effective continuum concept (cf. self-consistent method, differential scheme, etc.). Also, carefully constructed, i.e. inspired by micromechanics, phenomenological damage models have a good chance for success in the pre-peak regime. As the external load increases, the evolving defects reach a certain threshold density at which their hitherto-dilute concentration (ordered state) is replaced by a large defect cluster (disordered state). The emergence of a single dominant cluster (crack band or macrocrack) is preceded by intensive cooperative action of defects involving their own interactions and interplay between the hot spots (stress concentrations) and weak links (cleavage planes, interfaces, etc.). The transition from an ordered state to a disordered state is a non-deterministic, non-local, non-linear and non-equilibrium process which requires different methods of analysis than those of continuum mechanics, [56]. Such methods are offered by the physics of critical phenomena - a branch of modern statistical physics dealing with the behavior of disordered systems. The most known and probably the most appealing theory of that kind is the percolation theory (e.g. [107]). Originally applied to transport phenomena like conduction and diffusion, the percolation theory turned out to be a powerful tool when applied to brittle damage and fracture problems. The aim of the percolation studies is twofold: (1) determination of percolation thresholds, i.e. critical defect densities at which infinite clusters are formed, and (2) disclosure of scaling laws for the transport properties in the vicinity of the percolation threshold. On the credit side, no simplifying assumptions with regard to crack shapes and sizes, distributions of weak spots, etc., are necessary for the percolation theory to be applicable. On the debit side, percolation theory relies heavily on large-scale numerical simulations requiring considerable computational work when determining the percolation thresholds and universal parameters needed in applications.

1. Micromechanics of rock inelasticity: tension

Consider an elastic plate (RVE) with N non-interacting, randomly distributed open microcracks under plane stress (Fig.1). The objective here is to formulate a micromechanical damage model whose basic ingredient is the behavior of a single microcrack in a homogeneous tensile stress field. The analysis is confined to the two-dimensional case, small elastic deformations and isothermal conditions.
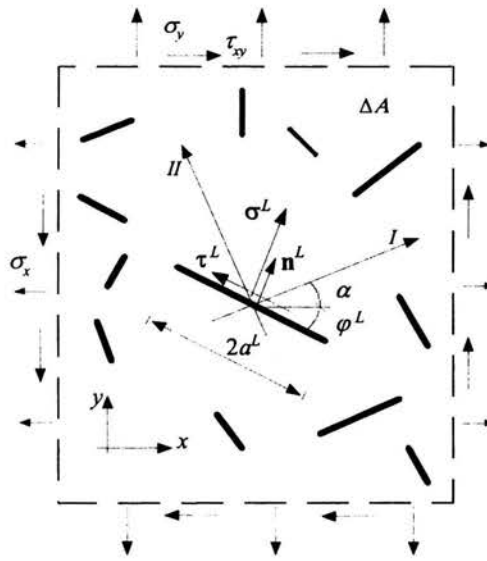

Figure 1: RVE with N randomly oriented microcracks in plane stress

1.1. Thermodynamic considerations

The Gibbs energy density for the RVE with N rectilinear microcracks is given by

$$\psi = \psi^0(\boldsymbol{\sigma}) + \Delta\psi(\boldsymbol{\sigma}, a) = \tfrac{1}{2}S^0_{ijkl}\sigma_{ij}\sigma_{kl} + \sum_{L=1}^{N} 2 \int_0^{a^L} \frac{\left(K_I^L\right)^2 + \left(K_{II}^L\right)^2}{E_0'\Delta A}\, da^L$$

(1.1)

where $\psi^0(\boldsymbol{\sigma})$ is the Gibbs energy density for the virgin matrix material, $\Delta\psi(\boldsymbol{\sigma}, a)$ is the change in that energy due to appearance of the microcracks, S^0_{ijkl} is the elastic compliance tensor of the matrix material, $E_0' = E_0$ in plane stress or $E_0' = E_0/\left(1 - \nu_0^2\right)$ in plane strain, E_0, ν_0 are Young's modulus and Poisson's ratio of the matrix material, K_I^L, K_{II}^L are the Mode I and Mode II stress intensity factors at the tip of the L-th microcrack, ΔA denotes the area of the representative surface element.

In the three-dimensional case all three SIFs must enter Eq. 1.1. It is a common modeling practice to assume the penny-shape geometry of real microcracks since for such cracks K_I, K_{II}, K_{III} are often available in analytical form.

In the plane case, K_I^L and K_{II}^L can be expressed as

$$K_I^L = \sigma^L\sqrt{\pi a^L}, \quad K_{II}^L = \tau^L\sqrt{\pi a^L}.$$

(1.2)

Using elementary relations between the tractions and the stress tensor, we get

$$\left(K_I^L\right)^2 + \left(K_{II}^L\right)^2 = \pi a^L \sigma_{ij}\sigma_{jk}n_k^L n_i^L.$$

(1.3)

For non-interacting microcracks, Eq. (1.1) can be integrated by use of Eq. (1.3):

$$\psi = \tfrac{1}{2}S^0_{ijkl}\,\sigma_{ij}\sigma_{kl} + \frac{\pi}{E_0'\Delta A}\sum_{L=1}^{N}\left(a^2 n_i n_k\right)^L \sigma_{ij}\sigma_{jk} =$$
$$= \tfrac{1}{2}S^0_{ijkl}\,\sigma_{ij}\sigma_{kl} + \frac{\pi}{E_0'}\,\omega_{ik}\,\sigma_{ij}\sigma_{jk}.$$

(1.4)

Incidentally, the second order symmetric tensor

$$\omega = \frac{1}{\Delta A}\sum_{L=1}^{N}\left(a^2\mathbf{n}\otimes\mathbf{n}\right)^L,$$

(1.5)

is the so-called crack density tensor, well-known in the damage mechanics literature (cf. [49, 71, 80, 113]). A dual derivation to Eq. (1.4) was presented in [52], where the elastic potential of a microcracked body was expressed via the crack opening displacements.

From Eq. (1.4), the general incremental form of the strain-stress relation reads

$$d\varepsilon_{ij} = \frac{\partial^2 \psi}{\partial \sigma_{ij}\, \partial \sigma_{kl}}\, d\sigma_{kl} + \frac{\partial^2 \psi}{\partial \sigma_{ij} \partial \omega_{kl}}\, d\omega_{kl}. \tag{1.6}$$

After respective differentiation operations, the final expression becomes

$$d\varepsilon_{ij} = -\frac{\nu_0}{E_0'} d\sigma_{kk}\delta_{ij} + \frac{1 + \nu_0}{E_0'} d\sigma_{ij} + \frac{2\pi}{E_0'}\left(\omega_{ik}d\sigma_{kj} + d\omega_{ik}\sigma_{kj}\right), \tag{1.7}$$

where the increment of the microcrack density tensor is given by

$$d\omega_{ik} = \sum_{L=1}^{N} \left(dN_{ik}a^2\right)^L + 2\sum_{L=1}^{N} \left(N_{ik}a\, da\right)^L. \tag{1.8}$$

The dyad $N_{ik} = n_i n_k$ characterizes the microcrack orientation. Note that for self-similar microcrack growth $d\mathbf{N} = 0$, in all other cases $d\mathbf{N} \neq 0$.

1.2. Kinetics of microcrack growth

Even though the initial orientation of microcracks is a random variable, only those microcracks which are perpendicular or nearly perpendicular to the maximum tensile stress direction will experience a substantial growth. The material inhomogeneity may somewhat disturb this picture since microcracks often become trapped by higher energy barriers (hard particles, grain boundaries, etc.) and are forced to change their path. Nevertheless, when zoomed out, a tortuous microcrack path generally follows the direction normal to the greatest principal stress direction, say σ_{II}. Guided by the LEFM solution, it is further assumed that inclined microcracks will evolve by sprouting curvilinear wings from the tips of the original microcracks. As the deformation goes on, the wings will promptly align themselves with the path normal to σ_{II}, Fig. 2.

Since the SIFs for the kinked microcrack are not available in closed analytical form, the following simplifications are made with regard to the

microcrack kinetics: (1) actual kinked microcrack is represented by a fictitious straight microcrack of the length $2(a + da)$ as shown in Fig. 2; (2) microcrack starts to grow if the stress and microcrack length projected on the plane normal to the maximum tensile stress direction attain threshold values yielded by the fracture condition.
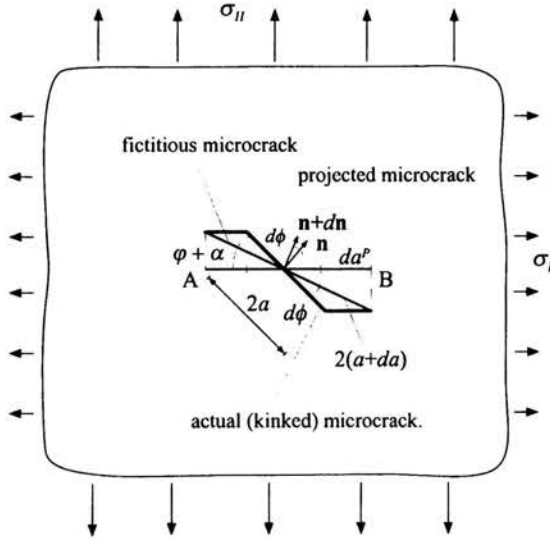

Figure 2: Model mechanism of inclined microcrack growth under biaxial tension

To include, albeit approximately, the effect of rock heterogeneity the classical Griffith criterion is replaced in the present model by the R-curve concept, namely

$$K_I = K_{Ic}(\Delta a).$$ (1.9)

A more precise form of Eq. (1.9) can be deduced from the available data of the crack resistance curve $K_{Ic}(\Delta a)$ for a particular rock (e.g. [46, 72, 73, 76, 101, 108]). These data suggest that a typical $K_{Ic}(\Delta a)$ curve for rocks (also concrete or mortar) is initially very steep and keeps rising until a steady state (plateau) is reached where the curve becomes flat, Fig. 3.

Based on the above reasoning, the following exponential form for the material function $K_{Ic}(\Delta a)$ is proposed [7]; see also [110].

$$K_{Ic}(\Delta a) = K_{cu} - (K_{cu} - K_{cl})\, e^{-\eta \dfrac{\Delta a}{a_0}},$$ (1.10)

where K_{cu}, K_{cl}, η are material constants and a_0 is the initial microcrack half-length. It should be stressed that the specific choice of the material function (1.10) is not crucial for the present model. Other possible expressions for $K_{Ic}(\Delta a)$, accounting for the energy barriers distribution, can be incorporated if required.

The slope of the $K_{Ic}(\Delta a)$ curve may vary with specimen's size and geometry - an undesirable effect. However, for small cracks in an infinite plate (cf. present model) the assumption of a size and geometry independent crack resistance curve is reasonable, [72].

In view of the introduced simplifications, Eq. (1.10) takes the form

$$\sigma_{ij}n_i^P n_j^P \sqrt{\pi a^P} = K_{cu} - (K_{cu} - K_{cl})\ e^{-\eta \Delta a^P/a_0^P}, \qquad (1.11)$$

where the superscript P stands for "projected" on the line AB in Fig. 3

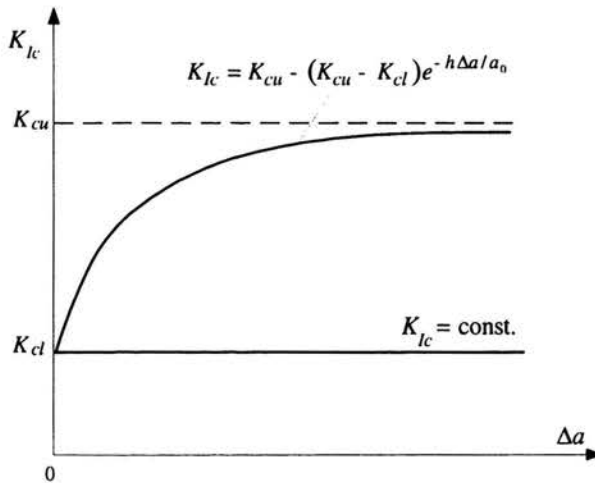Figure 3: Material function $K_{Ic}(\Delta a)$

From Eq. (1.11) the stress tensor and microcrack length are related as

$$d\sigma_{ij}N_{ij}^P = \frac{1}{\sqrt{\pi(a^P)^3}}\left[(K_{cu}-K_{cl})\ e^{\eta(1-a^P/a_o^P)}\left(\eta+\tfrac{1}{2}\right) - \tfrac{1}{2}K_{cu}\right]da^P,$$

$$\qquad (1.12)$$

where $N_{ij}^P = n_i^P n_j^P$.

The use of a rotating microcrack (cf. Fig. 2) involves a change in the microcrack orientation represented by the tensor dN_{ik}, namely

$$dN_{ik} = d\phi \left(N_{il}\nu_{lk} + \nu_{kl}N_{li} \right), \quad \nu_{lk} = \begin{bmatrix} 0 & 1 \\ -1 & 0 \end{bmatrix}. \tag{1.13}$$

Finally, the present model is completed by two geometrical relations:

$$da^P = \frac{da}{\cos(\varphi + \alpha)}, \qquad d\phi = \frac{da}{a} tg(\varphi + \alpha). \tag{1.14}$$

1.3. Illustrative example

A simple case of an RVE with a single microcrack under uniaxial tension will now be considered. The microcrack is perpendicular to the applied stress direction and it remains so as the load increases (self-similar growth). In this case the Gibbs energy density can rigorously be expressed as

$$\psi(\sigma, a) = \frac{\sigma^2}{2E_0} + 2\int_0^a \frac{K_I^2}{E_0\,\Delta A}\,da = \frac{\sigma^2}{2E_0}\left(1 + \frac{2\pi a^2}{\Delta A}\right). \tag{1.15}$$

Introduce dimensionless variables and material constants defined as follows

$$\tilde{\sigma} = \sigma/\sigma_0, \quad \tilde{\varepsilon} = \varepsilon/\varepsilon_0, \quad \tilde{a} = a/a_0, \quad \kappa = \frac{2\pi a_0^2}{\Delta A}, \quad \gamma^* = \frac{K_{cu}}{K_{cl}} \geq 1. \tag{1.16}$$

The microcrack growth condition Eq. (1.11) can be recast into a simple form

$$\tilde{\sigma} = \frac{1}{\sqrt{\tilde{a}}}\left[\gamma^* + (1-\gamma^*)\,e^{\eta(1-\tilde{a})}\right]. \tag{1.17}$$

Finally, the strain-stress relation follows from Eqs. (1.6), (1.15)-(1.17) as

$$d\tilde{\varepsilon} = \frac{1}{1+\kappa}\left[1 + \kappa\tilde{a}^2 + 4\kappa\tilde{a}^2 \frac{\gamma^* - (\gamma^* - 1)\,e^{\eta(1-\tilde{a})}}{(\gamma^* - 1)\,e^{\eta(1-\tilde{a})}(2\eta\tilde{a}+1) - \gamma^*}\right]d\tilde{\sigma}. \tag{1.18}$$

Note that κ can be interpreted as a microcrack density parameter. It can be deduced that for non-interacting microcracks κ should not exceed 0.1 (cf. [35]).

The stress-strain curves in the integrated form obtained from Eq. (1.18) are shown in Fig. 4. Qualitatively these curves correctly reflect the linear and hardening regimes. In the present form, the model does not aspire, though, to handle the softening regime.
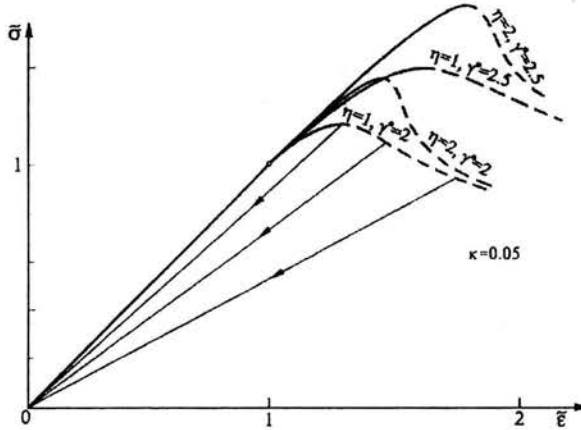

Figure 4: Predicted stress-strain curves in uniaxial tension for some values of η, γ^*

The specific expression (1.10) for the fracture toughness function $K_{Ic}(\Delta a)$ emphasizes the role of material inhomogeneity and inelastic processes in the neighborhood of the microcrack tip. It leads eventually to nonlinear stress-strain curves closely matching the shape of the experimental curves. Note, however, that an alternative microcracking scenario is often invoked. It assumes that K_{Ic} is constant while the observed nonlinear behavior results from sequential activations and arrests of the preexisting microcracks, [34, 58, 109].

2. Micromechanics of rock inelasticity: compression

The rock-like materials loaded in compression may deform according to different micromechanisms. For porous brittle materials, the pore-squeezing mechanism (Fig. 5_a) is often employed to account for the appearance and growth of tension microcracks parallel to the direction of maximum compressive stress, [98]. Other idealizations, based on K_I-solutions, identify bending of elongated inclusions (Fig. 5_b) or mismatch in the elastic constants of material constituents (Fig. 5_c) as potential sources of brittle microcracking, [53]. Also, the mechanism shown in Fig. 5_d is invoked when investigating compressive damage in concrete (cf. [34, 84].
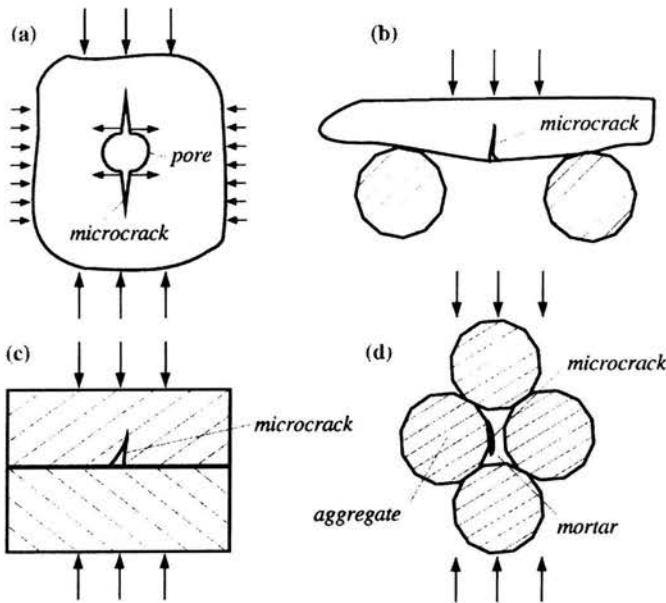

Figure 5: Several mechanisms of microcrack nucleation and growth under compression: (a) pore-squeezing (b) bending of elongated inclusion (c) mismatch in elastic constants (d) squeezing out of aggregates

2.1. Sliding microcrack mechanism

The sliding crack mechanism (Fig. 6) originated in Brace and Bombolakis, [15], and pursued thereafter by many authors (e.g. [8, 29, 33, 45, 48, 50, 53, 64, 65, 77, 81, 94, 98, 115]) is considered to be one of the major sources of rock inelasticity. It seems to capture most of the characteristics of the pre-peak response of rocks under compressive stresses. Apparently, it is for this versatility that it has been so widely used in rock mechanics. On the other hand there had been a long debate whether this mechanism actually occurs in real brittle materials. Some authors argued that the SEM observations do
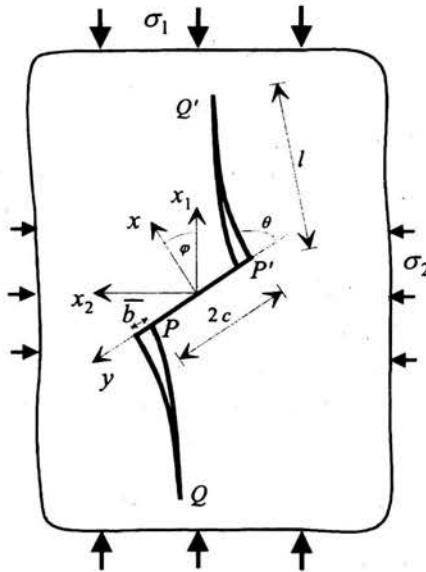

Figure 6: Sliding microcrack model of brittle deformation under biaxial compression

not support the existence of winged microcracks but seem to favor complex configurations of tensile microcracks propagating from different sources. Recent data from the AE tests do indicate that both tensile and shear events occur during brittle rock deformation, [70, 117].

For compact and relatively homogeneous rocks such as granite, this mechanism indeed seems to be a major contributor to inelastic deformation. However, more sophisticated experimental techniques and problem-oriented experimental programs are still necessary to settle that dispute.

2.2. Constitutive model

A key hypothesis of the Rice, [91, 92], thermodynamic framework is that every irreversible process of quasi-static deformation over a statistically homogeneous material sample under macroscopically homogeneous strain and temperature may be viewed as a sequence of (fictitious) constrained equilibrium states at which internal variables $\xi_1, \xi_2, \ldots, \xi_n$ are somehow frozen so as to have the same values as in the actual state. Within this framework Rice, [91], derived a fundamental *micro-macro* formula relating the increments of internal microscopic variables to the inelastic portions of the macroscopic strain increments:

$$d^i \varepsilon_{ij} = \frac{1}{V_0} \sum_\alpha \frac{\partial f_\alpha (\sigma, H)}{\partial \sigma_{ij}} \, d\xi_\alpha, \qquad (2.1)$$

where H denotes the current collection of values of $\xi_1, \xi_2, \ldots, \xi_n$ characterizing the current state of arrangement of the material constituents within the volume V_0 of an RVE; f_α is the set of thermodynamic forces conjugate to ξ_α.

The basic premise of Rice's approach, stating that material response be purely elastic when internal variables are held constant, is satisfied for frictional microcracks as well. No energy is dissipated if the slip displacements and the wing microcrack lengths are fixed through appropriate constraints. Hence, if the total strain increment is decomposed as

$$d\varepsilon = d^e \varepsilon + d^i \varepsilon = \mathbf{M}{:}d\sigma + d^i \varepsilon, \qquad (2.2)$$

then its inelastic part is derivable from (2.1). The instantaneous compliance tensor M_{ijkl} is given by

$$M_{ijkl} = \left. \frac{\partial^2 \psi (\sigma, H)}{\partial \sigma_{ij} \partial \sigma_{kl}} \right|_{H \; fixed}, \qquad (2.3)$$

so that M_{ijkl} is symmetric on interchange of ij and kl (diagonal symmetry). For open microcracks, the instantaneous compliance $\mathbf{M}$ coincides with the secant (effective) compliance $\mathbf{S}$ which is symmetric and anisotropic, [44]. It should be noted that at fixed microcrack lengths, $\mathbf{M}$ is nothing else but the unloading compliance. This is so because open cracks are usually assumed to close perfectly upon unloading. However, for frictional sliding on closed

microcracks the secant compliance matrix is non-symmetric, (e.g. [48, 52]) and the elastic potential defined as in Eq. (2.3) does not exist. The secant effective compliance is not the unloading compliance due to frictional effects. In conclusion, all basic relations of the Rice thermodynamic framework remain valid except that the instantaneous compliance $\mathbf{M}$ is not the secant compliance anymore. It is just an auxiliary concept which can be expressed in terms of $\mathbf{M}^o$ and the wing microcrack length l, [6].

The nucleation and growth of tension wings are induced by the wedging action of the frictional sliding on the surrounding material. In order to make the analytical model tractable, the curvilinear wings will be represented by the equivalent straight ones whose orientation θ is to be determined by maximizing $K_I(\theta)$ at a given straight wing length l. Consequently, the curved trajectory of the wing tip will be modeled as a sequence of positions of the straight wing cracks rotating around the corner points P or P' by the angle for which K_I reaches a maximum.

The Gibbs energy density due to N non-interacting winged microcracks in the RVE is [8]

$$\Delta\psi(\boldsymbol{\sigma}, H) = \frac{N}{A_0}\left[\int_{-c}^{c}\int_{0}^{b(y)}\tau_{xy}(\boldsymbol{\sigma}, b)db\,dy + 2\int_{0}^{l}G(\boldsymbol{\sigma}, l, \theta)\,dl\right]$$
$$= \frac{N}{A_0}\left[2c\int_{0}^{\bar{b}}\tau_{xy}(\boldsymbol{\sigma}, \bar{b})d\bar{b} + \frac{1}{E_0'}2\int_{0}^{l}(K_I^2 + K_{II}^2)\,dl\right], \qquad (2.4)$$

where G is the elastic energy release rate, $\bar{b} = \int_{-c}^{c}b(y)dy$ is the average slip displacement, and E_0' has already been defined in Eq. (1.1). The integrated form of (2.4), although analytic, is rather lengthy and is not displayed here.

The inelastic change of ψ reads

$$d^i\psi = \frac{\partial\psi}{\partial\bar{b}}d\bar{b} + \frac{\partial\psi}{\partial l}dl + \frac{\partial\psi}{\partial\theta}d\theta =$$
$$= \frac{N}{A_0}\left[\tau_{xy}2c\,d\bar{b} + 2Gdl + \frac{\partial}{\partial\theta}\left(2\int_{0}^{l}Gdl\right)d\theta\right] = \frac{N}{A_0}\sum_{\alpha=1}^{3}f_\alpha d\xi_\alpha. \qquad (2.5)$$

From Eq. (2.5), the microfluxes and the conjugated thermodynamic forces

for a single microcrack are

$$f_1 = \tau_{xy}2c, \ d\xi_1 = d\bar{b}; \ f_2 = G, \ d\xi_2 = dl; \ f_3 = \int\limits_0^l \frac{\partial G}{\partial \theta} dl, \ d\xi_3 = d\theta. \quad (2.6)$$

The explicit expressions for f_1, f_2, f_3 are contingent on the actual shear stress τ_{xy} on PP' and the stress intensity factors K_I and K_{II} at the wing tips.

Using stress superposition and balancing the forces projected on the line PP' in the cross section $QPP'Q'$ (Fig. 6), it follows that

$$\tau_{eff}2c - \left[\sigma_{11}\cos^2(\theta+\varphi) + \sigma_{22}\sin^2(\theta+\varphi) + \tau_{12}\sin(2(\theta+\varphi))\right]2l\sin\theta +$$
$$+\left[\frac{1}{2}(\sigma_{11}-\sigma_{22})\sin(2(\theta+\varphi)) - \tau_{12}\cos(2(\theta+\varphi))\right]2l\cos\theta + 2\hat{F}_{el}(\bar{b},l) = 0,$$
$$(2.7)$$

where $\hat{F}_{el}(\bar{b},l) = F_{el}^I\sin\theta + F_{el}^{II}\cos\theta$ is the sum of the projections on PP' of the appropriate elastic crack-closing forces F_{el}^I, F_{el}^{II} in Mode I and Mode II, respectively. The F_{el}^I, F_{el}^{II} are the forces in elastic material due to stress singularities at the crack tip. In view of Eqs. (2.6) and (2.7), the force conjugated to $d\bar{b}$ becomes

$$f_1 = \tau_{xy}^\infty 2c - \sigma_{11}2l\sin\varphi\cos(\theta+\varphi) + \sigma_{22}2l\cos\varphi\sin(\theta+\varphi) +$$
$$- \tau_{12}2l\cos(\theta+2\varphi) - 2\hat{F}_{el}(\bar{b},l) \ . \quad (2.8)$$

The exact solution for the SIFs at the tips of curvilinear wings can be obtained only numerically [45, 64]. However, numerous closed-form approximations of K_I and K_{II} are available in the literature. They can be arranged in two classes: displacement-driven models (e.g. [81]) and force-driven models (e.g. [43, 53, 77, 115]). The displacement-driven and the force-driven models of the basic mechanism are depicted in Fig. 7. Recently, Lehner and Kachanov, [68], published an exhaustive overview of all available approximations of the SIFs for the winged crack.

In the displacement-driven model, the rectilinear wings are pushed sideways by a rigid wedge whose dimensions are determined by the preexisting microcrack length $2c$ and the varying slip displacement $\bar{b}$. Here, the SIFs involve complete elliptic integrals of the first and second kind $K(k)$ and $E(k)$, cf. [111]. These SIFs are not expressible by means of analytic

functions except for the special case of a semi-infinite wedge, which would correspond to a pair of separate straight wing microcracks not interacting with each other. This might be a realistic approximation only for the initial phase of kinking when the wings are very small $(l \ll c)$.
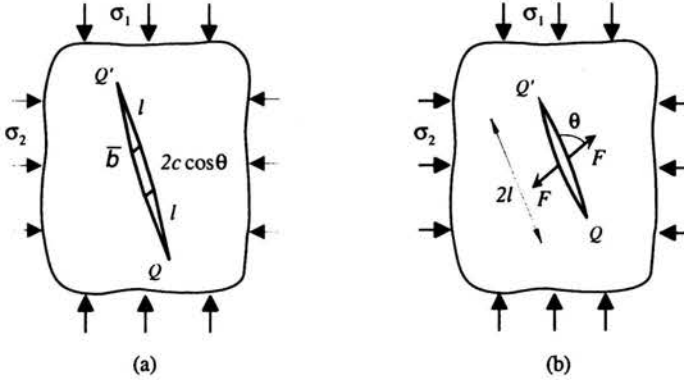

Figure 7: Two models of sliding crack mechanism: (a) displacement driven, (b) force driven

For separate wings, there is no wing-wing interaction thus the modulus k equals zero and the SIFs at the tips Q and Q' are (e.g. [111])

$$K_I \left(\bar{b}, l, \sigma\right) =$$

$$= \frac{E_0' \bar{b} sin\theta}{2\sqrt{2\pi \left(l + l^{**}\right)}} + \sqrt{\frac{\pi l}{2}} \left[\sigma_{11} cos^2 \left(\theta + \varphi\right) + \right.$$

$$\left. + \sigma_{22} sin^2 \left(\theta + \varphi\right) + \tau_{12} sin \left(2 \left(\theta + \varphi\right)\right)\right],$$

$$K_{II} \left(\bar{b}, l, \sigma\right) =$$

$$= -\frac{E_0' \bar{b} cos\theta}{2\sqrt{2\pi \left(l + l^{**}\right)}} - \sqrt{\frac{\pi l}{2}} \left[\tau_{12} cos \left(2 \left(\theta + \varphi\right)\right) + \right.$$

$$\left. - \tfrac{1}{2} \left(\sigma_{11} - \sigma_{22}\right) sin \left(2 \left(\theta + \varphi\right)\right)\right],$$

$$(2.9)$$

where $l^{**} = 0.27\,\pi^2 c/32$ is the nucleus wing length introduced in [81] to get the correct behavior of Eq. (2.9) in the short wing limit.

Strictly speaking, the original sliding microcrack is displacement-driven. The SIFs at the wing tips are directly proportional to the relative slip of the slanted microcrack faces. However, during the forward- or backsliding, the wedging action on the wings may equivalently be seen as force-driven. Then, the wedging effect can be represented by two collinear

splitting forces $F = -2c\tau_{eff}$, Fig. 7_b. If the curvilinear wings are further approximated by the straight cracks whose orientation θ_c satisfies the condition $K_I(\theta_c) \to max$, the estimates of the SIFs are, [43]:

$$
\begin{aligned}
K_I(F,l,\boldsymbol{\sigma}) = \\
&= \frac{F\sin\theta}{\sqrt{\pi\,(l+l^*)}} + \sqrt{\pi l}\,\big[\sigma_{11}\cos^2(\theta+\varphi)+ \\
&\quad +\sigma_{22}\sin^2(\theta+\varphi) + \tau_{12}\sin(2(\theta+\varphi))\big]\,, \\
K_{II}(F,l,\boldsymbol{\sigma}) = \\
&= \frac{-F\sin\theta}{\sqrt{\pi\,(l+l^*)}} - \sqrt{\pi l}\,\big[-\tfrac{1}{2}(\sigma_{11}-\sigma_{22})\sin(2(\theta+\varphi))+ \\
&\quad + \tau_{12}\cos(2(\theta+\varphi))\big]\,,
\end{aligned}
\tag{2.10}
$$

where $l^* = 0.27\,c$ plays the same role as l^{**} in the displacement-driven model.

The inelastic strains induced by the coupled effects of frictional sliding along preexisting flaw, wing extension, and its simultaneous rotation can now be computed. It should be kept in mind that the wing rotation is just a by-product of the adopted model of the curvilinear wing tip trajectory. The wing length itself is calculated from the $K_I = K_{Ic}$ condition. The inelastic strain increments are obtained from the fundamental relation (2.1) using the derived microstructural thermodynamic forces Eqs (2.6), (2.8) and the approximate expressions for the SIFs, Eqs (2.9), (2.10). It is essential that the conjugate forces f_α be symmetrized in the components of $\boldsymbol{\sigma}$ and all three components of the stress applied at infinity be included when performing differentiation in Eq. (2.1). This differentiation is to be carried out at fixed H, i.e. at $\tilde{b}$, $\tilde{l}$ held constant, where $\tilde{b} = \bar{b}/c$ and $\tilde{l} = l/c$. In the force-driven model (Fig. 7b), the effect of frictional sliding along PP' is represented by the action of two collinear splitting forces F. Once the internal variables $\tilde{b}$, $\tilde{l}$ are held frozen, so are the splitting forces F. Therefore, the physical law (i.e. friction) for F should not be substituted in the expressions for the SIFs prior to the differentiation operation in Eq. (2.1).

The total strain increment consists of the following terms

$$
d\varepsilon_{ij} = d^e\varepsilon_{ij} + d\varepsilon_{ij}^s + d\varepsilon_{ij}^c + d\varepsilon_{ij}^\theta,
\tag{2.11}
$$

which represent, in order of appearance, the contributions from elasticity, frictional sliding, wing extension and wing rotation. Limited by space, the

explicit expressions for the individual terms in Eq. (2.11) are here omitted and can be found elsewhere, [5].

The constitutive framework is made complete by specifying the kinetic equations for the rates $d\xi_i/dt$. Since no crack-crack interaction is included, it suffices to consider kinetic equations for the three internal variables $\tilde{b}, \tilde{l}, \theta$ of a single winged microcrack. Consequently, the overall strains may be estimated afterwards using a simple averaging procedure that sums up the individual contributions of all active microcracks while accounting for their spatial distribution.

In general, the slip displacement $\tilde{b}$ is to be computed from the forward- or backsliding activation condition, the wing length $\tilde{l}$ from the winged microcrack growth condition, the orientation angle θ of the equivalent straight microcrack from the maximization of K_I with respect to θ. The rates $\dot{\tilde{b}}, \dot{\tilde{l}}, \dot{\theta}$ expressed in terms of the applied stress rates $\dot{\sigma}_{ij}$ are obtained imposing the consistency requirements upon the above conditions.

The sliding activation condition is obtained by combining the equilibrium (2.7) and the Mohr-Coulomb condition for frictional glide:

$$
\begin{aligned}
\Omega^s = & \ \sigma_{11} \left[cos\varphi \ (sin\varphi - \mu \, cos\varphi) + \tilde{l} \, cos\,(\theta + \varphi) \, sin\varphi \right] \\
& - \sigma_{22} \left[sin\varphi \ (cos\varphi + \mu \, sin\varphi) + \tilde{l} sin\,(\theta + \varphi) \, cos\varphi \right] \\
& + \tau_{12} \left[cos2\varphi + \mu \, sin2\varphi - \tilde{l} \, cos\,(\theta + 2\varphi) \right] + \tau_c + c^{-1} \, \hat{F}_{el} = 0.
\end{aligned}
\tag{2.12}
$$

As noticed by Moss and Gupta, [77], it is difficult to determine $\hat{F}_{el}$ because the stress-COD expression for the entire kinked microcrack is not available. Consequently, some approximate solutions were sought. For example, Moss and Gupta, [77], neglected the initial slit ($c \to 0$) and considered two limiting cases: $\theta \to 90°$ (locally Mode I microcrack) and $\theta \to 0°$ (Mode II microcrack). Assuming that the wings grow parallel to σ_1 direction (i.e. $\theta + \varphi = \pi/2$), these authors obtained from Eq. (2.12) that

$$
\hat{F}_{el} = \bar{b} \, E_0'/4.
\tag{2.13}
$$

Estimation of the elastic restoring forces makes the computation of $\tilde{b}$ straightforward. Furthermore, the kinetic equation for $\dot{\tilde{b}}$ can now be derived from the sliding activation Eq. (2.12) by time differentiation. For the

sake of completeness, we recall also an alternative algorithm for computing $\tilde{b}$ proposed by Nemat-Nasser and Obata [81]. These authors did not analyze the equilibrium of the slanted microcrack but assumed that $\tilde{b}$ can be derived from a duality of K_I factors upon requiring that K_I of the displacement-driven model Eq. (2.9) be equal to that of the force-driven model Eq. (2.10) when the sliding mechanism is active.

The remaining kinematic variables $\tilde{l}$ and θ are obtained as functions of stresses from the following conditions

$$K_I = K_{Ic}, \quad \frac{\partial K_I}{\partial \theta} = 0 \,, \tag{2.14}$$

where K_I is given by Eq. (2.9) or (2.10) depending on the considered model. Kinetic relations for $\dot{\tilde{l}}$ and $\dot{\theta}$ follow from Eq. (2.14) by time differentiation. The resulting equations are algebraically quite involved thus were solved numerically using the symbolic algebra softwares. In the long-wing limit, these equations take simpler forms and for the uniaxial compression are even solvable analytically.

The above equations were derived for loading regime. Unloading in case of sliding microcracks is a complex phenomenon since any reduction of applied stresses does not necessarily mean elastic unloading. The energy may locally be dissipated on backsliding or wing growth of some microcracks despite the fact that the overall stress is actually decreasing. Also, unloading on some sliding microcracks may happen if the load path is changed, the load itself being not necessarily reduced. Possible cases of unloading are discussed in detail in [8], where the corresponding $d\varepsilon_{ij} - d\sigma_{ij}$ equations are also derived.

2.3. Application

The developed constitutive model was implemented numerically using *Mathematica* and applied to reproduce the test data of Zoback and Byerlee, [118], on Westerly granite under unconfined compression. Westerly granite is a relatively homogeneous and nearly brittle compact rock. For these reasons it was selected for the verification of the present analytical model.

At distributed damage, the overall stresses and strains may fairly well be approximated by simple area averages of the contributions of individual sliding microcracks. Assuming a finite number of specific orientations of the

preexisting microcracks, the average strain increment may be computed as

$$d\bar{\varepsilon}_{ij} = \frac{1}{R} \sum_{r=1}^{R} d\varepsilon_{ij}(\varphi_r, \, \omega_0(\varphi_r)) \,, \tag{2.15}$$

where R is the number of considered orientations (φ_r). In the example to follow, an isotropic distribution of preexisting microcracks is assumed, i.e. all microcrack orientations are likely to appear. From symmetry arguments, the shear strains in the global coordinate system disappear.

The material constants used in computations were identified as follows:

$$E_0 = 58GPa, \nu_0 = 0.23, \sigma_{uc} = -204MPa, \mu = 0.65, \tau_c = 12MPa,$$
$$K_{Ic} = 0.7MPa\sqrt{m}, \omega_0 = 0.375, R = 90, c = 5 \, 10^{-4}m. \tag{2.16}$$

The numerical values for E_0, ν_0, σ_{uc} were read off from the test curves in [118]; see also [22]; σ_{uc} denotes the highest compressive stress recorded in loading. The friction coefficient μ, the average initial microcrack half-length c, and the fracture toughness K_{Ic} were estimated using the values for Westerly granite reported in [22, 47, 77, 81]. No data were available for Westerly granite with regard to the initial microcrack density parameter $\omega_0 = \frac{Nc^2}{A_0}$. The selected value provided the best fit with the data, and is rather consistent with those assumed in [77, 81].

The solid curves depicted in Fig. 8 represent $(\sigma - \varepsilon)$ equations predicted by the present model while dots are the data measured by

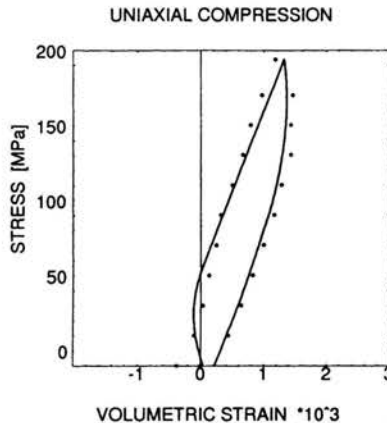

UNIAXIAL COMPRESSION

VOLUMETRIC STRAIN *10^3

Figure 8: Predicted stress-volumetric strain curves (solid lines) vs. test data on Westerly granite from unconfined compression (from [8])

Zoback and Byerlee, [118], on cylindrical specimens in uniaxial compression. Note that material parameters used in computations are well documented in the referenced literature. Typically of micromechanical models, the present formulation contains no fitting parameters.

2.4. Interaction of microcracks under compression

Consider two closed cracks in an infinite, linear elastic plate (Fig. 9) with the local (crack-attached) coordinate systems (x^L, y^L) and the global coordinate system (x_1, x_2). To facilitate drawing, only two cracks are shown
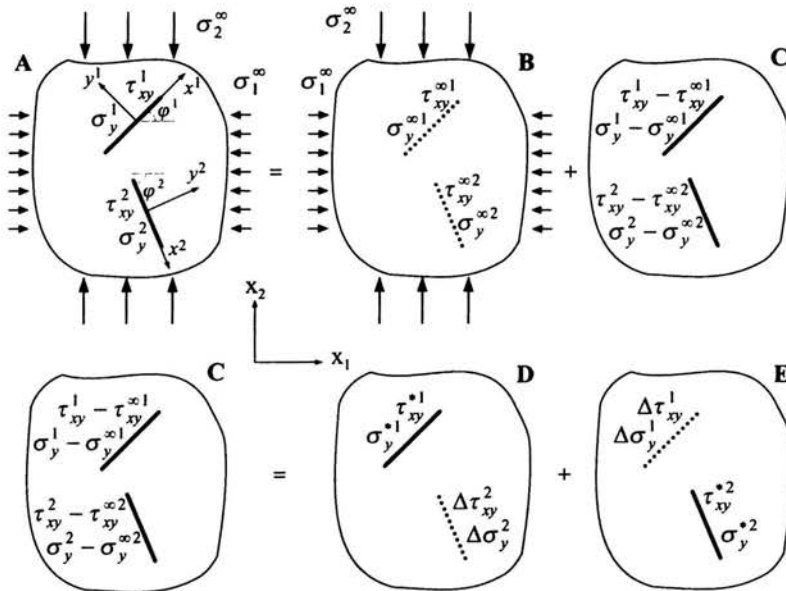

Figure 9: Superposition of stresses for interacting frictional cracks in infinite, linear elastic plate under compression

but the ensuing equations are formulated for an arbitrary 2D crack array $(L = 1, 2, ..., N)$. The actual (contact) shear and normal stresses existing on the faces of L-th crack are denoted by τ^L_{xy}, σ^L_y. The boundary-value problem A can trivially be decomposed into two subproblems B, C. On the other hand, the problem C can be represented as a superposition of N subproblems, each involving only a single crack but subjected to *unknown* shear and normal stresses τ^{*L}_{xy}, σ^{*L}_y. The adopted sign convention is that of

continuum mechanics, i.e. compression is viewed negative. Consequently, for closed frictional cracks it follows from Fig. 9 that

$$\tau_{xy}^{*L} = \tau_{xy}^{L} - \left(\tau_{xy}^{\infty L} + \Delta\tau_{xy}^{L}\right), \tag{2.17}$$

$$\sigma_{y}^{*L} = \sigma_{y}^{L} - \left(\sigma_{y}^{\infty L} + \Delta\sigma_{y}^{L}\right), \tag{2.18}$$

where $\tau_{xy}^{\infty L}$, $\sigma_{y}^{\infty L}$ are the resolved shear and normal stresses in the continuous material along the line of L-th crack; $\Delta\tau_{xy}^{L}$, $\Delta\sigma_{y}^{L}$ are the interaction terms, i.e. shear and normal stresses generated by all other cracks along the line of L-th crack in the continuous material. As long as the crack remains closed, it holds $\sigma_{y}^{*L} = 0$. Otherwise, $\sigma_{y}^{*L} = -\left(\sigma_{y}^{\infty L} + \Delta\sigma_{y}^{L}\right)$.

A necessary prerequisite for computation of the SIFs is determination of the loading of crack faces $(\tau_{xy}^{*L}, \sigma_{y}^{*L})$. Once τ_{xy}^{*L}, σ_{y}^{*L} are known, the SIFs can be computed according to the well-known formulas, [111]:

$$K_{I}^{L}\left(\pm c^{L}\right) = \frac{1}{\sqrt{\pi\,c^{L}}} \int\limits_{-c^{L}}^{c^{L}} \sqrt{\frac{c^{L}\pm\zeta}{c^{L}\mp\zeta}}\, p^{*L}\left(\zeta\right) d\zeta, \tag{2.19}$$

$$K_{II}^{L}\left(\pm c^{L}\right) = \frac{1}{\sqrt{\pi\,c^{L}}} \int\limits_{-c^{L}}^{c^{L}} \sqrt{\frac{c^{L}\pm\zeta}{c^{L}\mp\zeta}}\, \tau^{*L}\left(\zeta\right) d\zeta, \tag{2.20}$$

where $p^{*L} = -\sigma_{y}^{*L}$, $\tau^{*L} = -\tau_{xy}^{*L}$ due to the sign convention and c^{L} denotes the half-length of a straight crack. For closed cracks only (2.20) is relevant.

In essence, the method devised in [51] for open cracks is based on the following *Ansatz*:

The unknown tractions induced on the considered crack by the presence of other cracks can be approximated by tractions that would have been acted on the considered crack if the other cracks were loaded by uniform average (normal and shear) tractions.

It is claimed now that irrespective of whether interacting cracks are open or frictional, the central assumption of the Kachanov method remains valid, i.e. the unknown crack interaction stresses $\Delta\sigma_{y}^{L}$, $\Delta\tau_{xy}^{L}$ are induced only by uniform average tractions (as yet unknown) acting on the other cracks' faces. A far-reaching consequence of this assumption is that it yields a functional form for the unknown stresses $\Delta\sigma_{y}^{L}$, $\Delta\tau_{xy}^{L}$ since the problem of a single

crack loaded by uniform tractions has analytical solution. Denote by P_{ij}^K and T_{ij}^K standard stress fields that are generated in the continuous material by the K-th crack loaded by uniform normal and shear tractions of *unit intensity*, respectively. These standard stress fields can be computed using a suitable Westergaard function (as it is done in this chapter) or can be found in textbooks on linear fracture mechanics. Hence, the crack interaction terms $\Delta\sigma_y^L$, $\Delta\tau_{xy}^L$, (generated in the continuous material) can be expressed in the following general form, [51],

$$\Delta\sigma_y^L = -n_i^{(L)} \left[P_{ij}^K \left\langle \sigma_y^{*K} \right\rangle + T_{ij}^K \left\langle \tau_{xy}^{*K} \right\rangle \right] n_j^{(L)}, \quad K, L = 1, ..., N; \ (K \neq L), \tag{2.21}$$

$$\Delta\tau_{xy}^L = -n_i^{(L)} \left[P_{ij}^K \left\langle \sigma_y^{*K} \right\rangle + T_{ij}^K \left\langle \tau_{xy}^{*K} \right\rangle \right] m_j^{(L)}, \quad K, L = 1, ..., N; \ (K \neq L). \tag{2.22}$$

Here, the sum convention applies to the repeated indices K while it does not apply to the indices placed in parentheses i.e. (L); $\mathbf{n}^L$, $\mathbf{m}^L$ are the crack-attached normal and tangential unit vectors; the bracket $\langle \rangle$ denotes the average value of the bracketed quantity.

The actual stresses τ_{xy}, σ_y induced by the frictional-cohesive contact on the crack faces are interrelated through a law of dry friction. A simple Coulomb-Mohr law is adopted for this purpose:

$$\tau_{xy}^L = \mp\tau_c \pm \mu\sigma_y^L, \tag{2.23}$$

where τ_c is the cohesion and μ is the coefficient of dry friction, both being positive constants. In Eq. (2.23) and the equations to follow, the upper signs hold for cracks oriented at $0 < \varphi^L < \frac{\pi}{2}$ while the lower ones for $-\frac{\pi}{2} < \varphi^L < 0$, Fig. 9.

From the above equations it follows that

$$\tau_{xy}^{*L} = \mp\tau_c \pm \mu\sigma_y^{\infty L} - \tau_{xy}^{\infty L} \pm \mu\,\Delta\sigma_y^L - \Delta\tau_{xy}^L, \qquad K, L = 1, 2, ..., N. \tag{2.24}$$

The averaging of Eq. (2.24) leads to

$$\left\langle \tau_{xy}^{*L} \right\rangle = \mp\tau_c \pm \mu\sigma_y^{\infty L} - \tau_{xy}^{\infty L} \pm \mu \left\langle \Delta\sigma_y^L \right\rangle - \left\langle \Delta\tau_{xy}^L \right\rangle, \tag{2.25}$$

where:

$$\left\langle \Delta\sigma_y^L \right\rangle = -\Lambda_{11}^{KL} \left\langle \sigma_y^{*K} \right\rangle - \Lambda_{12}^{KL} \left\langle \tau_{xy}^{*K} \right\rangle, \tag{2.26}$$

$$\left\langle \Delta\tau_{xy}^L \right\rangle = -\Lambda_{21}^{KL} \left\langle \sigma_y^{*K} \right\rangle - \Lambda_{22}^{KL} \left\langle \tau_{xy}^{*K} \right\rangle, \tag{2.27}$$

where Λ_{ij}^{KL} are the Kachanov, [51], transmission factors (interaction matrices) defined as follows

$$\left.\begin{aligned}
\Lambda_{11}^{KL} &= n_i^{(L)} \left\langle P_{ij}^K \right\rangle^{(L)} n_j^{(L)} \\
\Lambda_{12}^{KL} &= n_i^{(L)} \left\langle T_{ij}^K \right\rangle^{(L)} n_j^{(L)} \\
\Lambda_{21}^{KL} &= n_i^{(L)} \left\langle P_{ij}^K \right\rangle^{(L)} m_j^{(L)} \\
\Lambda_{22}^{KL} &= n_i^{(L)} \left\langle T_{ij}^K \right\rangle^{(L)} m_j^{(L)}
\end{aligned}\right\} \quad (K \neq L) \qquad (2.28)$$

$$\Lambda_{ij}^{KL} = 0; \quad (K = L). \qquad (2.29)$$

For convenience, the notation of the transmission factors in Eqs (2.28)-(2.29) has been slightly changed (cf. [5]) as compared with that in the original paper ([51]). For example, Λ_{21}^{KL} denotes the average shear stress (lower index 2) on crack L due to unit normal stress (lower index 1) on crack K. Note that to compute the transmission factors the standard stress fields generated by the uniformly loaded K-th crack have to be integrated along the line of L-th crack. For a given configuration of N cracks this is usually done by numerical integration.

For closed frictional cracks $\sigma_y^{*L} = 0$, thus the following system of N linear equations is obtained from Eqs (2.25)-(2.29), [9],

$$\left(\delta^{KL} \pm \mu \Lambda_{12}^{KL} - \Lambda_{22}^{KL}\right) \left\langle \tau_{xy}^{*K} \right\rangle = \mp \tau_c \pm \mu \sigma_y^{\infty L} - \tau_{xy}^{\infty L}, \quad (K, L = 1, 2, ..., N). \qquad (2.30)$$

The right hand side of Eq. (2.30) specifies the remote loading conditions and the friction-cohesion resistance on each crack's faces. In other words, it represents the effective (net) shear stress that drives the crack sliding. The crack array geometry and the influence of friction on the transmission of shear stresses are reflected by the left hand side. The system of equations (2.30) with the transmission factors (2.28), (2.29) and a given load $(\sigma_y^{\infty L}, \tau_{xy}^{\infty L})$ on crack faces constitute the governing system of linear algebraic equations from which the average shear stresses $\left\langle \tau_{xy}^{*K} \right\rangle$ can be computed.

If the average values of shear stresses $\left\langle \tau_{xy}^{*K} \right\rangle$ are known, it is straightforward to compute the whole distribution of τ_{xy}^{*K}. From Eq. (2.24),

when combined with Eqs (2.22) and (2.23), it follows that

$$\tau_{xy}^{*L} = \mp \tau_c \pm \mu \sigma_y^{\infty L} - \tau_{xy}^{\infty L} + n_i^{(L)} T_{ij}^K \langle \tau_{xy}^{*K} \rangle \left(\mp \mu n_j^{(L)} + m_j^{(L)} \right). \qquad (2.31)$$

Finally, combining Eqs (2.31) and (2.21), the K_{II} factors for interacting frictional cracks read, [9],

$$K_{II}^L(+c) = \sqrt{\pi c^{(L)}} \left(\tau_{xy}^{\infty(L)} \pm \tau_c \mp \mu \sigma_y^{\infty(L)} \right) +$$

$$+ \frac{\langle \tau_{xy}^{*K} \rangle}{\sqrt{\pi c^{(L)}}} \left[n_i^{(L)} \left(\int_{-c^L}^{c^L} \sqrt{\frac{c^L + \zeta}{c^L - \zeta}} T_{ij}^K d\zeta \right) \left(\pm \mu n_j^{(L)} - m_j^{(L)} \right) \right]$$

$$K_{II}^L(-c) = \sqrt{\pi c^{(L)}} \left(\tau_{xy}^{\infty(L)} \pm \tau_c \mp \mu \sigma_y^{\infty(L)} \right) +$$

$$+ \frac{\langle \tau_{xy}^{*K} \rangle}{\sqrt{\pi c^{(L)}}} \left[n_i^{(L)} \left(\int_{-c^L}^{c^L} \sqrt{\frac{c^L - \zeta}{c^L + \zeta}} T_{ij}^K d\zeta \right) \left(\pm \mu n_j^{(L)} - m_j^{(L)} \right) \right]$$

$$(2.32)$$

To evaluate the predictive capability of the present model, the basic equations (2.30)-(2.32) have been implemented numerically. The numerical algorithm is relatively simple except for the weighted integrals in Eq. (2.32) which required some special treatment.

In Figs 10-12 the present solutions are compared with the 'exact' numerical ones obtained by means of the *BEM* for some test examples. The normalized K_{II} factors vs. the relative distance of crack tips d/c are plotted for frictionless ($\mu = 0$) and frictional contact ($\mu = 0.3$) on crack faces. The normalization factor K_{II0} is the stress intensity factor for the respective single crack under a given load with all other cracks absent.

All figures clearly show that accuracy of the extended Kachanov method is excellent even at very small distances between the crack tips. There are at least two reasons for this accuracy. First of all, we have been dealing here with somewhat biased, though important, situations of straight cracks and distributed loading on crack faces. For such situations the Kachanov scheme is best suited. Secondly, the exact formulas for the SIFs (2.19), (2.20) involve the unknown crack-face tractions only in an integral sense. This is in tune with the basic assumption of the Kachanov method stating that it is the average tractions that contribute most to the SIFs. As for 3D crack
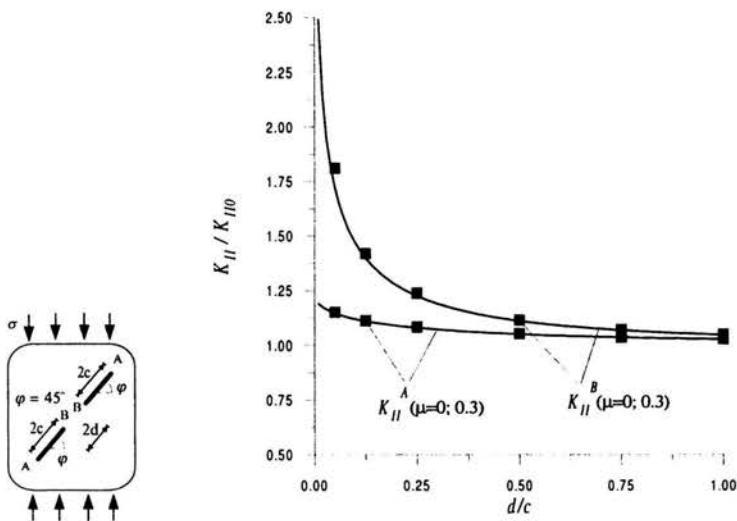
Figure 10: Two collinear cracks under uniaxial compression. Normalized K_{II} factors vs. relative distance of crack tips for $\mu = 0;\ 0.3$ and $\tau_c = 0$. Solid lines depict present solution, squares - BEM solution
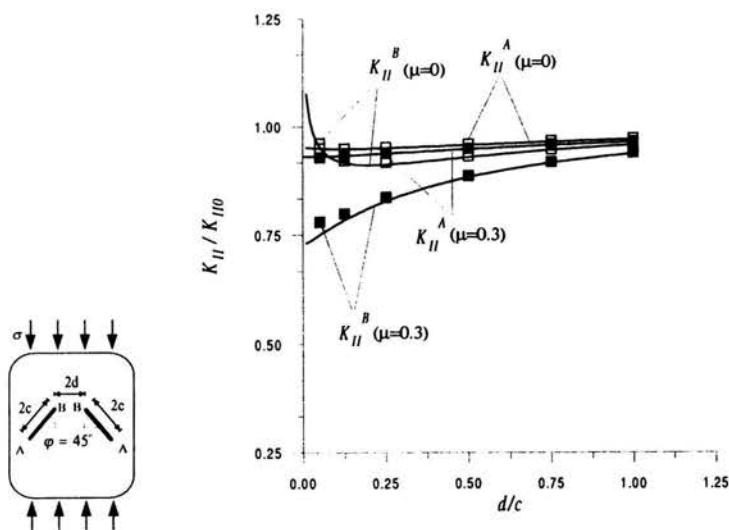

Figure 11: Two symmetrically inclined cracks under uniaxial compression. Normalized K_{II} factors vs. relative distance of crack tips. Solid curves - present solution, squares - BEM data for $\mu = 0$, $\mu = 0.3$ at $\tau_c = 0$

configurations, it is known from the analysis of open cracks ([52]) that the method performs even better than in 2D cases.
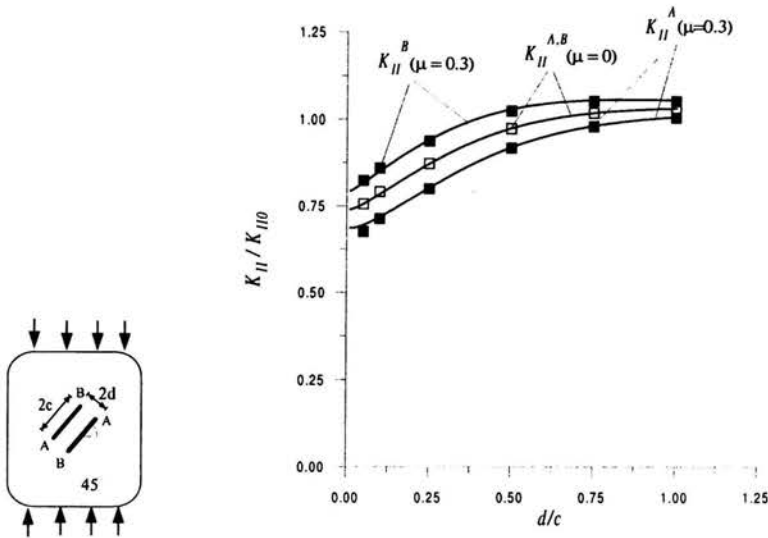

Figure 12: Two stacked cracks under uniaxial compression. Normalized K_{II} factors vs. relative distance of crack tips. Solid curves - present solution, squares - *BEM* data, for $\mu = 0$, $\mu = 0.3$ at
$$\tau_c = 0$$

It seems thus legitimate to state that the Kachanov method of direct crack interaction analysis performs exceedingly well for frictional cracks under compression for non-process (frozen) patterns of straight cracks. However, if the interacting cracks start to grow, it is clear that their growth cannot be considered as self-similar. Hence, the key element of the method, being the standard stress fields for straight cracks, ceases to be valid.

3. Chemo-micromechanics of corrosive damage in concrete

Recent successes in micromechanical modeling, relating microstructure of a material to its macroresponse provide a strong stimulus for application of the same methodology to the problem of corrosive damage. The main objective here is to investigate the relation existing between the performance of a structure and the chemical composition of the material-ambient system. Gradual degradation of a concrete or mortar specimen exposed to sulfate attack, common to many environments, seems to be a particularly suitable example for the illustration of the proposed chemo-micromechanical modeling.
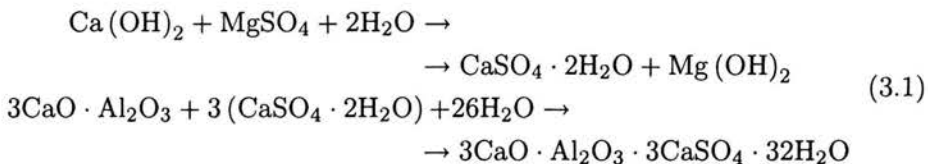
3.1. Chemical reaction

Sulfate attack on concrete may manifest in a variety of ways depending on concentration of SO_4, composition of concrete, source and kind of sulfate. The following forms of sulfate attack are distinguished, [18]:

- sulfate attack associated with ettringite and/or gypsum formation,
- sulfate attack associated with brucite formation and decalcification,
- thaumasite formation.

Thaumasite ($CaCO_3 \cdot CaSO_4 \cdot CaSiO_3 \cdot 15H_2O$) formation is generally associated with concretes exposed to carbonate and sulfate at low temperatures and pH level above 10.5, [99]. Formation of thaumasite occurs as a result of the reaction between calcium silicate hydrate (C-S-H) and SO_4^{2-}, CO_2 or CO_3^{2-} and water. The rate of thaumasite formation drops off markedly at temperatures somewhere between 15°C and 20°C. The damage of concrete due to the thaumasite formation is usually profound and is mainly due to the decomposition of the C-S-H phase, resulting in a loss of strength.

The magnesium sulfate attack on concrete at low concentration of $MgSO_4$, produces gypsum and ettringite, [1]. However, if sulfate concentration exceeds 0.75% the formation of brucite and decalcification takes the upper hand. In the initial stage of magnesium sulfate attack brucite layer is formed. The brucite formation consumes a high amount of $Ca(OH)_2$, supplied by the hydrated paste. When the available $Ca(OH)_2$ is depleted, the pH of pore solution gets lowered. In order to maintain its stability, the C-S-H can release the $Ca(OH)_2$ to the surrounding solution, thus increasing the pH. This process ultimately contributes to the decalcification of the C-S-H, and the loss of cementitious structure. In the advanced stage, the Ca ions in the C-S-H can be completely replaced by the Mg ions leading to the formation of magnesium silicate hydrate (M-S-H) which is non-cementitious.

Ettringite and gypsum formation are associated with concretes exposed to magnesium and sodium sulfate solution at strength below 0.75%. Ettringite and gypsum are the primary products of the chemical reaction between a sulfate-bearing solution and cement hydrated or anhydrate particles. Ettringite formation will be described on example of magnesium sulfate attack. This attack is initiated by the reaction between $MgSO_4$ and $Ca(OH)_2$. It is followed by the reaction of gypsum with some alumina-bearing phases like tricalcium aluminate ($3CaO \cdot Al_2O_3$, or C_3A in cement industry nomenclature) or monosulfate ($3CaO \cdot Al_2O_3 \cdot 3CaSO_4 \cdot 32H_2O$) to form secondary ettringite, as shown in the following reactions:

$$
\begin{aligned}
Ca(OH)_2 + MgSO_4 + 2H_2O \rightarrow \\
\rightarrow CaSO_4 \cdot 2H_2O + Mg(OH)_2 \\
3CaO \cdot Al_2O_3 + 3(CaSO_4 \cdot 2H_2O) + 26H_2O \rightarrow \\
\rightarrow 3CaO \cdot Al_2O_3 \cdot 3CaSO_4 \cdot 32H_2O
\end{aligned}
\tag{3.1}
$$

The first reaction $(3.1)_1$ is a through-solution reaction since it proceeds in the aqueous medium filling the pores. Calcium hydroxide dissolved from the walls of pores reacts with the sodium sulfate from the ambient solution to form gypsum ($CaSO_4 \cdot 2H_2O$) and sodium oxide which precipitates from the solution. The difference in volume between gypsum (reaction product) and $Ca(OH)_2$ (reactant) is readily accommodated by the original porosity of mortar and the additional space released by the dissolved $Ca(OH)_2$. The second reaction $(3.1)_2$, involving tricalcium aluminate, newly formed gipsum, and water needed to form the ettringite, is often assumed to be of the solid-

liquid or topochemical type. It occurs directly on the surface of C_3A crystal and may generate large swelling pressures if the space available locally is not sufficient for undisturbed growth of the ettringite crystal. Comparing the volumes of reactants and products it follows that one volume of C_3A yields 8.2 volumes of solid ettringite. Consequently, the growing ettringite crystal exerts pressure on the side of pores which results in local tensile stresses of a high magnitude. The local tensile stresses may, eventually, become sufficient to induce microcraking and expansion of the concrete specimen.

The kinetics of above reactions depends on the sequence of two processes. Firstly, the reactant particles must be brought into contact by diffusion of external sulfate-bearing water through concrete. Subsequently, a chemical reaction between particles in contact may take place. The model of kinetics of ettringite formation discussed below was proposed by Pommersheim and Chang, [90]. They considered a spherical C_3A grain, with an initial radius r_{a0}, exposed to a steady supply of sulfate ions. As the reaction progresses, a layer of ettringite forms on the outside of the shrinking part of the C_3A grain. The hydration of C_3A in presence of gypsum is modeled as steady diffusion process. Therefore, from Fick's I law and stoichiometric analysis of reactions (3.1) it follows that:

$$\frac{dr_a}{dt} = -D_e \phi_e \frac{c r_e}{3 r_a \left(r_e - r_a \right) d_a} \tag{3.2}$$

$$\frac{dr_e}{dt} = \left(1 - \frac{d_a}{(1 - \phi) d_e} \right) \left(\frac{r_a}{r_e} \right)^2 \frac{dr_a}{dt} \tag{3.3}$$

where D_e=0.5·10⁻¹² m²/s is the diffusivity of ettringite, ϕ_e=0.18 is the porosity of ettringite layer, c (mol/m³) is the actual molar concentration of sulfate, d_a=11261.3 mol/m³ and d_e=1379.1 mol/m³ are the molar density of C_3A and ettringite, respectively; r_a and r_e are the radius of C_3A and ettringite grains, respectively. Solving these equations with initial conditions $r_a = r_e = r_{a0}$ at $t = 0$, one obtains the dependence of r_e and r_a on (Figs 13, 14).

As can be seen from these figures, the rate of ettringite production is rapid initially, and gets slower as time elapses. It is the consequence of the increasing thickness of ettringite layer. Note that the time necessary to fully convert the C_3A grain into ettringite is very short in comparison with time of sulfate ions diffusion through concrete. Consequently, since the sulfate-induced degradation of concrete is typically a process taking months, it seems

reasonable to conclude that the actual rate-controlling mechanism is the diffusion of sulfate ions through the mortar matrix, the rate of ettringite production being of secondary importance.
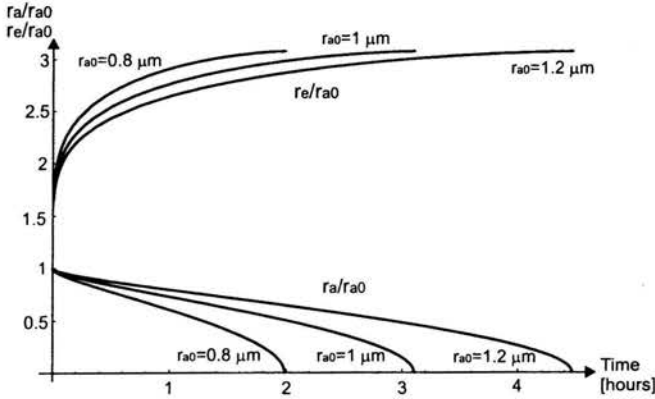

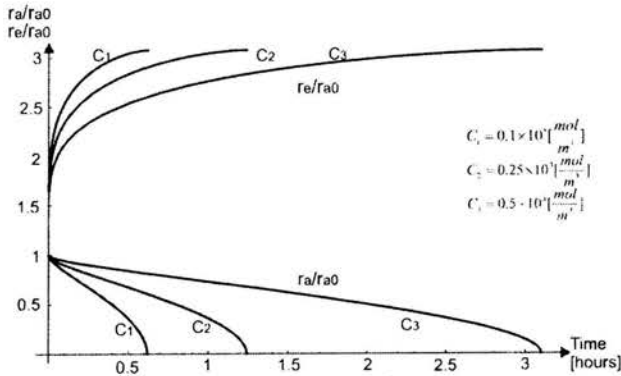Figure 13: Ettringite formation at constant concentration of SO_4, $c=0.1 \cdot 10^3$ [mol/m^3]

Figure 14: Ettringite formation at constant C$_3$A radius $r_{a0}=1$ μm

The volumetric strain due to expansion of a spherical ettringite particle reads, [59]

$$\varepsilon^v = (d - 1) \left[1 - (r_a/r_{a0})^3 \right]. \tag{3.4}$$

The maximum expansion coincides with the completion of the reaction, i.e. at $r_a = 0$. Hence,

$$\varepsilon^v_{max} = d - 1 .\tag{3.5}$$

3.2. Diffusion with chemical reaction

In this study, a hardened concrete or mortar is assumed to be initially saturated by chemically inert water. At $t = 0$, the specimen is immersed in a pool of water containing a constant concentration c_0 of sulfate ions. The sulfate ions diffuse through the mortar driven by the concentration gradient. As they do so they encounter in their path calcium dioxide particles, react, form gypsum, and eventually ettringite as suggested by Eq. (3.1).

Spatial and temporal distribution of sulfate ions within the specimen is governed by a modification of Fick's second law (e.g. [32])

$$\frac{\partial c}{\partial t} = \nabla \cdot (\mathbf{D}_{eff} \nabla c) + R(c)\tag{3.6}$$

where $c(\mathbf{x}, t)$ is the concentration of the diffusing substance, $\mathbf{D}_{eff}(\mathbf{x}, t)$ the effective diffusivity tensor, and $R(c)$ the rate of the reaction per unit volume (sink term). The reaction rate represents the time rate of change in the concentration of sulfate ions consumed in the chemical reaction with the active ingredients of the cement paste.

From the material balance for the double-decomposition reaction (3.1) the sink term in Eq. (3.6) is equal to the negative tripled rate of ettringite formation is

$$R(c) = \frac{dc^R}{dt} = -3\frac{dc_e}{dt}\tag{3.7}$$

As was already discussed, the formation of ettringite during the hydration of cement was found to be controlled by diffusion. However, the mechanism by which ettringite is formed in the course of external sulfate attack on the hardened cement paste differs significantly from its formation during the hydration of cement. Before the sulfate ions can react with the C_3A particles remote from the main pores, they have to find their way to these particles through the network of micropores. Moreover, only a part of the C_3A grain is likely to be in immediate contact with the aggressive solution, and not all of the pores are suitable for the ettringite build-up, [40]. Since a rigorous microstructural modeling of this process seems to be extremely complex and

non-deterministic, it will simply be assumed that that the rate of ettringite formation is proportional to the current amounts of the reactants (cf. [24, 59], i.e.

$$\frac{dc_e}{dt} = kcc_a = kc\left(c_a^0 - c_e\right) \tag{3.8}$$

where c_a^0 is the initial concentration of C_3A in the hardened cement paste, k is the rate constant of the double decomposition reaction (3.1) depending on the size, tortuosity and connectivity of the micropores.

Substitution of Eq. (3.8) into Eqs (3.7) and (3.6) leads to a partial differential equation

$$\frac{\partial c}{\partial t} = \nabla \cdot (\mathbf{D}_{eff} \nabla c) - 3kc\left(c_a^0 - c_e\right) \tag{3.9}$$

The associated boundary condition is that $c = c_0$ on the surfaces exposed to the water with constant concentration of sulfate ions. Initial condition is that $c = 0$ within the specimen at $t = 0$.

3.3. Transport properties

The problem of the determination of material properties is typically and efficiently resolved within the effective medium approximation framework (e.g. [78, 82]). The most popular and most frequently used among the first-order effective media approximations is the so-called self-consistent method (SCM). The SCM is based on the assumptions that: (a) the mean stress field of each inclusion is identical and equal to the far-field stress, (b) external fields of each inclusion weakly depend on the exact positions of other inclusions.

3.3.1. Effective medium regime

- *Diffusivity*

The diffusivity $\mathbf{D}$ is a structural parameter exhibiting strong dependence on the tortuosity of the fluid path through the solid, [28]. In a virgin hardened cement paste the diffusivity depends on the pore structure, i.e. the distribution and connectivity of pores $\phi(r)$ having different radii r. Assuming the pores to be perfectly random with respect to their orientation and width, the virgin (undamaged) hardened cement paste may be considered to be of isotropic diffusivity. It will be assumed that the accessible porosity ϕ and

isotropic diffusivity D_0 of the virgin hardened cement paste are known. As the microcracks within the specimen nucleate and grow, the tortuosity of the fluid path decreases and the effective diffusivity increases. This problem has been discussed in the past on many levels of rigor and sophistication (e.g. [4, 36, 97]).

Salganik's model, [97], developed within the SCM approximation, considers each inclusion to be of ellipsoidal shape, the concentration gradients within the inclusion $s_i^I = \partial c/\partial x_i$ are homogeneous whenever the far-field concentrations are homogeneous as well. In the case of randomly oriented penny-shaped microcracks of radius a, the effective diffusivity can be cast into a simple formula, [97],

$$D = D_0 \left(1 + \frac{32}{9}\,\omega\right) \tag{3.10}$$

where

$$\omega = N \left\langle a^3 \right\rangle \tag{3.11}$$

is the Budiansky-O'Connell microcrack volume density parameter (micromechanical damage parameter).

- *Elastic constants*

In the case considered, the mortar matrix contain both ettringite inclusions and microcracks growing from the matrix-inclusion interfaces. The effect of the water inundating the specimen is neglected.

Comparison between overall specimen expansions (of up to 0.4%) and expansions of a single ettringite inclusion ($d = 9.96$) leads to a conclusion that the actual volume density of expanding inclusions is rather small. Even though self-consistent estimates for elastic moduli of a solid (mortar) containing a dilute suspension of spherical inclusions (ettringite crystals) are available (e.g. [21]), it seems sufficient for the present purposes to invoke the much simpler mixture rule. Consequently, the effective elastic modulus of the mortar matrix with ettringite inclusions is

$$E_0 = \left(1 - f^I\right) E_{cp} + f^I E_e \tag{3.12}$$

where $f^I = \sum V^I/V$ is the total volume fraction of ettringite crystals in the mortar RVE, while the indices "cp" and "e" stand for cement paste and ettringite, respectively.

The local stress concentration near the inclusions significantly exceeds the average macrostresses associated with the beam-column action of the specimen. Hence, the orientation of microcracks emanating from the interface will be perfectly random. Assuming that all microcracks are penny-shaped, the self-consistent estimate for the overall elastic modulus E of the mortar matrix containing a dilute concentration of ettringite inclusions and microcracks is, [19]

$$\frac{E}{E_0} = 1 - \frac{16}{45} \frac{\left(1 - \nu^2\right)\left(10 - 3\nu\right)}{\left(2 - \nu\right)} \omega \qquad (3.13)$$

and, implicitly, for the overall Poisson ratio ν

$$\omega = \frac{45}{16} \frac{\left(\nu_0 - \nu\right)\left(2 - \nu\right)}{\left(1 - \nu^2\right)\left[10\nu_0 - \nu\left(1 + 3\nu_0\right)\right]} \qquad (3.14)$$

where ω is again defined by (3.11), and "0" denotes the uncracked matrix (with etrringite crystals, though).

3.3.2. Percolation regime

Expressions (3.10) for the diffusivity and (3.13) for the elastic parameters are valid only for dilute concentration of defects located far enough from each other to prevent their interaction. However, as the microcracks grow in size, the distance separating adjacent microcracks will decrease. As the defect clusters grow, they will invariably start dominating both the diffusivity and stiffness of the specimen. Since the location of inclusions and the ensuing shapes of the microcrack clusters are random, the determination of transport properties of the solid at this stage using traditional applied mechanics methods is not possible.

The behavior of systems in the stage characterized by the emergence of a defect cluster spanning an observed region exhibits certain universal aspects. The percolation theory represents an eminently suitable framework for studies of systems in the vicinity of the percolation threshold defined as emergence of a spanning cluster.

- *Diffusivity*

Formula (3.10) is valid only if the microcracks are far apart. However, as soon as a cluster traversing the specimen forms, some of the liquid

will be transported through it as well. The percolation threshold ω_c at which a spanning cluster, composed of randomly oriented penny-shaped microcracks of equal radii, connects two opposite surfaces of the sample has been determined by numerical simulations, [20] as

$$\omega_c = N_c a^3 \approx 0.182 \tag{3.15}$$

where N_c is the critical number (per unit volume) of penny-shaped microcracks of radius a connected into an uninterrupted path through the specimen.

The scaling law for the diffusivity attributable to the spanning cluster is, [107]

$$D_p \propto (\omega - \omega_c)^\mu \tag{3.16}$$

where $\mu \approx 2$ is a universal exponent (dimensional invariant independent of microstructure, established by numerical simulation) for a three-dimensional case.

In order to account for the diffusion through the matrix containing non-intersecting penny-shaped microcracks and the conductance through the spanning cluster, it seems reasonable to postulate that a parallel connection between the two transport phenomena exists, i.e. that the overall diffusivity is, [59]

$$D = D_0 \left(1 + \frac{32}{9}\omega\right) + D_p \tag{3.17}$$

where

$$D_p = D_0 \frac{(\omega - \omega_c)^2}{\omega_{ec} - \omega} \quad \text{for} \quad \omega_c < \omega < \omega_{ec} \tag{3.18}$$

is the diffusivity through the spanning cluster, satisfying the conditions

$$D_p = 0 \text{ for } \omega < \omega_c \quad \text{and} \quad D_p = \infty \text{ for } \omega > \omega_{ec} \tag{3.19}$$

Expressions (3.18)-(3.19) for diffusivity D_p acknowledge existence of two different universal classes of problems having different percolation thresholds: (a) $\omega = \omega_c$ (conduction percolation threshold) at which a spanning cluster traverses the volume creating a worm-hole in the material, and (b) $\omega = \omega_{ec}$ (elastic or rigidity percolation threshold) at which a cluster of cracks transect the volume. At the elastic percolation threshold the macrostiffness vanishes and it is, for simplicity, assumed that the diffusion becomes practically instantaneous.

● *Stiffness*

The SCM expressions for elastic moduli (3.13), (3.14) are valid for dilute concentration of microcracks. The elastic percolation represents a different universal class necessitating additional numerical and experimental simulations to determine the elastic percolation threshold ω_{ec} at which the elastic modulus $E \to 0$, and the scaling law is $E \propto (\omega_{ec} - \omega)^f$ as $\omega \to \omega_{ec}$. Numerical simulations, [104], indicate that

$$\omega_{ec} = \langle Na^3 \rangle_c \approx 0.712 \tag{3.20}$$

and

$$E \propto (\omega_{ec} - \omega)^{4.1} \tag{3.21}$$

The effective-medium response in which E is a linear function of ω, Eq. (3.13), and the response at impending percolation during which E is a strongly nonlinear function of ω, Eq. (3.21), are separated by a crossover regime. The functional dependence $E(\omega)$ within the crossover regime requires significant numerical simulations which have still to be performed. However, it is interesting that a self-consistent estimate of the elastic percolation threshold is

$$\omega_{ec}^{SC} = \tfrac{9}{16} \approx 0.8\,\omega_{ec} \tag{3.22}$$

for $\nu = 0$ in Eq. (3.13). The function $E(\omega)$ and its first four derivatives vanish at $\omega = \omega_{ec}$. Thus, the function is so flat in the vicinity of ω_{ec} that $E(\omega_{ec}^{SC}) \approx 0.1E_0$. Consequently, the assumption that $E(\omega_{ec}^{SC}) \approx 0$ will be well within the overall accuracy. Indeed, the results of Lemieux et al., [69], and Sahimi and Goddard, [96] indicate that the elastic percolation threshold of articulated lattices is surprisingly close to the value obtained from the effective medium theories, i.e. assuming that SCM is valid up to the point at which the elastic modulus E (3.13) vanishes. Experimental and numerical data supplied by Sieradzki and Li, [103], Benguigui, [12, 13] lend further credence to this assumption, indicating that the actual magnitude of the elastic modulus at the critical microcrack density, (estimated using the SCM) is approximately 10% of its original value E_0. Finally, numerical simulations for lattices, [39, 57], confirm the validity of the assumption that the SCM estimates of the elastic percolation threshold are quite accurate. In conclusion it seems reasonable to assume that the SCM estimate for the elastic modulus, Eq. (3.14), is valid within the entire range $0 < \omega < 9/16$.

3.4. Stress-strain relationship

The present task consists in determining the compliance of the hardened cement paste containing an ensemble of expanding crystals and an ensemble of microcracks. At this point, it will be assumed that all expanding crystals are spherical in shape and all microcracks are penny-shaped. Consistent with the analysis in the preceding section, it will again be assumed that the defect concentration is low to moderate, rendering their direct interaction inconsequential. The incubation period, i.e. the time lag between the onset of the reaction and the onset of the specimen expansion, [83], resulting from the initial unconstrained growth of the ettringite crystal within the pore, is short in comparison to the time needed for diffusion and will be neglected. It will also be assumed that relatively small pore pressures have no appreciable effect on the stress-strain relationship.

3.4.1. Inhomogeneous inclusion

Consider first the stress and strain fields surrounding an inhomogeneous inclusion (expanding ettringite crystal) occupying domain Ω, embedded into a homogeneous and isotropic effective medium (cement paste containing a dilute concentration of randomly oriented defects). Assuming the inclusion to be spherical in shape, the free expansion strain attributable to the difference between volumes of reactants and reaction products is

$$\varepsilon_{ij}^r = \tfrac{1}{3}\varepsilon^v \delta_{ij} \tag{3.23}$$

where ε^v is given by the expression (3.4) or (3.5), while δ_{ij} is the Kronecker symbol.

Denote the total eigenstrain within the inclusion by

$$\varepsilon_{ij}^{**} = \varepsilon_{ij}^r + \varepsilon_{ij}^* + \varepsilon_{ij}^t \tag{3.24}$$

where ε_{ij}^* is the equivalent eigenstrain resulting from the disparity in elastic moduli between the matrix and inclusion; $\varepsilon_{ij}^t = \alpha T^r \delta_{ij}$ is the strain due to the thermal expansion associated with the heat released or consumed during the course of chemical reactions and crystal growth. As usual, α is the coefficient of thermal expansion (depending on ω) and T^r the temperature difference measured from some reference level (taken as $T^r = 0$). A similar reaction taking place during the hydration of cement in fresh cement paste is strongly

exothermic, releasing substantial thermal energy of 1.45 J/g of the reaction product (cf. [74]).

In the absence of mechanical tractions on external surfaces of the specimen, the expression for eigenstrain (3.24) can be derived as in Mura, [78], in the form

$$\varepsilon_{kk}^{**} = \frac{3\,(1-\nu)\,K^I}{(1+\nu)\,K^I - (4\nu - 2)\,K}\varepsilon_{kk}^r + \alpha\,T^r = \beta\varepsilon_{kk}^r + \alpha\,T^r \qquad (3.25)$$

where the superscript I indicates reference to the inclusion while the non-indexed parameters characterize the surrounding effective continuum. All off-diagonal components of the strain tensor are equal to zero as a result of spherical symmetry. The inclusions grow in a degrading matrix containing a large number of microcracks, approximated by the effective continuum. Since the parameters of the effective continuum depend on the microcrack density ω, the eigenstrain (3.25) can be written as

$$\varepsilon_{kk}^{**} = \beta\,(\omega)\,\varepsilon_{kk}^r + \alpha\,T^r \qquad (3.26)$$

where the expressions for the bulk modulus $K\,(\omega)$ and the Poisson's ratio $\nu\,(\omega)$ of the effective continuum (contained in β) can be obtained from (3.13), (3.14). Since the heat released during the exothermic reactions (3.1) is proportional to the mass of the reaction product expression (3.26) can finally be recast in a simple form

$$\varepsilon_{kk}^{**} = \beta\,(\omega, T^r)\,\varepsilon_{kk}^r \qquad (3.27)$$

However, since no reliable estimate of the heat released during reactions (3.1) is available, the thermal eigenstrain will be neglected at this stage of the model development. The uniform radial pressure within the expanding homogeneous, elastic inclusion must be proportional to the eigenstrain (3.27). Hence, from Eq. (3.5) and (3.27), the maximum pressure (coinciding with the completion of the reaction) exerted on the surrounding matrix is

$$p = K^I\varepsilon_{kk}^{**} = K_e\beta\,(\omega)\,(d-1) \qquad (3.28)$$

where $K^I = K_e$ is the bulk modulus of inclusion (ettringite).

The actual ettringite-pore interaction is simplified for the modeling purposes as shown in Fig. 15. Assuming that initially a small notch exists at the inclusion-matrix interface, the K_I can be approximated as

$$K_I \approx pR^2/\sqrt{\pi a^3} \qquad (3.29)$$

where R is the pore radius, a the microcrack half-length, p is the swelling pressure. Since the SIF is not available for the three-dimensional case considered, expression (3.29) is derived using the solution for the line load as the influence function ([79], p. 671).
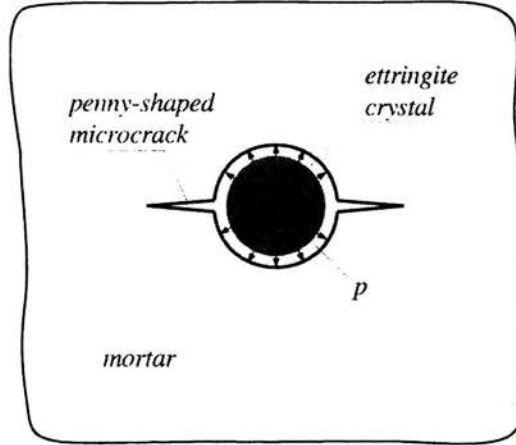

Figure 15: Two-dimensional visualization of spherical ettringite crystal growing within a spherical pore

For a constant radius $R = r_{a0}$ of the C$_3$A inclusion, it follows from the Griffith criterion that

$$a = r_{a0} \sqrt[3]{p^2 r_{a0}/ \left(\pi K_{Ic}^2 \right)} \tag{3.30}$$

where K_{Ic} is the fracture toughness of the hardened cement paste. As soon as the microcrack opens, the pressure exerted by growing ettringite grain is released. Additional inclusion expansion is needed for further microcrack growth. From Eq. (3.30) it can be seen that the microcrack is stable because $\partial K_I / \partial a < 0$. From Eq. (3.28), the terminal radius of a circular microcrack formed around a spherical C$_3$A grain is, [59]

$$a = r_{a0} \sqrt[3]{\left[\beta \left(\omega \right) \left(1 - d \right) K_e \right]^2 r_{a0}/ \left(\pi K_{Ic}^2 \right)} \tag{3.31}$$

3.4.2. Stress-strain relationship on macroscale

Once the local stress and strain fields around an inhomogeneous inclusion have been determined, the magnitudes of the respective macrofields at

each material point of the effective continuum can be computed through a homogenization process (i.e. by averaging these fields over the tributary RVE). Consider, to this end, a volume V containing a reasonably dilute concentration of spherical inclusions having a total volume of $V^I = f^I V$. The relation mapping the macrostresses $\boldsymbol{\sigma}$ on macrostrains $\boldsymbol{\varepsilon}$ can be written combining contributions of beam-column action and inhomogeneous inclusions:

$$\boldsymbol{\varepsilon} = \mathbf{S}(\omega):\boldsymbol{\sigma} + \boldsymbol{\varepsilon}^I \tag{3.32}$$

where $\mathbf{S}(\omega)$ is the effective compliance tensor reflecting ettringite build-up and microcracking. Since the volume average of stress perturbations in the matrix (induced by ettringite crystal expansions) must by definition vanish, the second term on the right-hand side of Eq. (3.32) involves only summation of eigenstrains over all inclusions:

$$\boldsymbol{\varepsilon}^I = f^I \boldsymbol{\varepsilon}^{**} \tag{3.33}$$

where f^I is the inclusion volume density and $\boldsymbol{\varepsilon}^{**}$ the eigenstrain given by Eq. (3.27).

Assuming perfectly random orientations of microcracks and random distribution of inclusions, the components of the effective tensor $\mathbf{S}(\omega)$ can be computed using expressions (3.13), (3.14) for the effective Young's modulus E and Poisson's ratio ν. Application of expression (3.32) requires, finally, formulation of a relation between the sulfate concentration $c(\mathbf{x}, t)$ obtained by solving Eq. (3.9) and the damage parameter $\omega(\mathbf{x}, t)$. As has been already shown, the actual reaction time is very small compared to the time of diffusion of sulfate ions through the mortar. Thus, on the diffusion time scale, the final microcrack length is attained instantaneously. Consequently, the rate of damage evolution defined by ω, Eq. (3.11), is proportional to the rate at which C₃A particles are activated.

From the solution of the diffusion-reaction equation it is possible to determine the molar concentration of the sulfate consumed to form etrringite crystals. Integrating the kinetic equation (3.8), we get

$$c^R(\mathbf{x}, t) = 3c_e(\mathbf{x}, t) = 3c_a^0 \left[1 - exp \left(-k \int_0^t c(\mathbf{x}, t)\, dt \right) \right] \tag{3.34}$$

Thus, the number of C₃A grains (per unit volume V) involved in the reaction with sulfate (3.34) is

$$N_a = c^R/\hat{m}_s = \left(c^R v_a \right) / 4\pi r_{a0}^3 \tag{3.35}$$

where $\hat{m}_s$ is the mass of magnesium sulfate (in moles) needed to convert completely a single particle of tricalcium aluminate into ettringite, r_{a0} and v_a are again the initial radius and molar volume of the C_3A crystal.

Using the relation (3.31) and the number of already reacted C_3A particles from Eq. (3.35), the damage parameter (3.11) can be cast into following implicit form

$$\omega = N_a a^3 = N_a \beta^2 (\omega) (d-1)^2 \frac{K_e^2 r_{a0}^4}{\pi K_{Ic}^2} \tag{3.36}$$

The final set of governing equations comprises the equilibrium, compatibility and boundary conditions.

3.5. Application

A set of data related to the expansion of mortar specimens exposed to a combined external attack of $MgSO_4$ and Na_2SO_4 has been provided by Ouyang et al., [85], who performed experiments in accordance with ASTM C1012 recommendations. It was observed that the rate of mortar expansion during external sulfate attack is an increasing function of time (see also [67]).

The ASTM C490 prismatic test specimen were placed in a mixed solution of 0.176 mol/l $MgSO_4$ and 0.176 mol/l Na_2SO_4. A tacit assumption is made that the action of magnesium sulfate and sodium sulfate on mortar are similar in the sense that both substances serve as sources for the aggressive ions SO_4^{2-}. In practice, magnesium sulfate is often more dangerous because it additionally decomposes hydrated calcium silicates (cf. [67]). On the other hand, it has been reported that sodium sulfate solution is more corrosive than magnesium sulfate solution if the calculated content of C_3A in the cement exceeds 9%, [14]. In the light of this information, the assumption of equal average influence of both substances on concrete corrosion seems reasonable.

In order to determine the actual initial concentration of C_3A available for the reaction with aggressive ions diffusing through the test specimen, it is first necessary to estimate how much of C_3A anhydride remains in the cement paste after the hydration process. Denoting by f_g the amount of gypsum (mass fraction) usually added to Portland cement clinker to avoid rapid setting, the initial molar concentration of tricalcium aluminate is

$$c_a^0 = \frac{M_{cm}}{m_a V} \left(f_a - f_g \frac{m_a}{3 m_g} \right) \tag{3.37}$$

where $f_a = (4.3\%,\ 7\%,\ 8.8\%,\ 12\%)$ is the mass fraction of C_3A in the cement as given in Ouyang et al., [85]. As before, m_a and m_g are the molar masses of C_3A and gypsum, M_{cm} is the mass of cement in $V = 1\ m^3$ of mortar. The ratio $(m_a/3m_g)$ in Eq. (3.37) results from the mass balance of reaction (3.1).

Consider now the diffusion equation (3.9) with the diffusivity defined by Eqs (3.17)-(3.19). To replicate the experimental trends it seems sufficient to assume the diffusion to be one-dimensional (across the thickness only). Therefore, from Eqs (3.9) and (3.17) we have

$$\frac{\partial \tilde{c}}{\partial \tilde{t}} = \frac{\partial}{\partial \tilde{x}} \left\{ \left[\tilde{D}_0 \left(1 + \tfrac{32}{9}\omega \right) + D_p \right] \frac{\partial \tilde{c}}{\partial \tilde{x}} \right\} - 3k\tilde{c} \left(\tilde{c}_a^0 - \tilde{c}_e \right) \tag{3.38}$$

In Eq. (3.38) and the equations to come, the following normalization is used:

$$\tilde{x} = x/w_0, \quad \tilde{c} = c/c_0, \quad \tilde{c}_e = c_e/c_0, \quad \tilde{c}^R = c^R/c_0, \quad \tilde{t} = t/T, \quad \tilde{D}_0 = \frac{D_0 T}{w_0^2} \tag{3.39}$$

with $T = 24h$. The initial and the boundary conditions are

$$\tilde{c}(\tilde{x},\ 0) = 0, \quad \tilde{c}(-1,\ \tilde{t}) = \tilde{c}(1,\ \tilde{t}) = 1, \quad \frac{\partial \tilde{c}}{\partial x}(0,\ \tilde{t}) = 0. \tag{3.40}$$

The governing equation (3.38) is highly nonlinear, rendering the analytical or approximate solutions not possible. Thus, it had to be solved numerically using finite difference method.

In the one-dimensional case considered, the $\sigma - \varepsilon$ relation (3.32) acquires a simple form

$$\varepsilon = \frac{\sigma}{E} + f^I \varepsilon^{**} \tag{3.41}$$

where E is the elastic modulus of the damaged hardened cement paste containing both the ettringite inclusions and the microcracks. The f^I is again the volume fraction of the C_3A particles in $1m^3$ of mortar, given as

$$f^I = \tfrac{4}{3} N_a \pi\, r_{a0}^3 \tag{3.42}$$

where N_a is calculated form Eq. (3.35).

Since the stress components τ_{xy} and σ_x vanish, and $\sigma_y = \sigma \neq 0$ depends only on x, equilibrium is automatically satisfied. The compatibility conditions (in stresses) reduce to

$$\frac{d^2}{d\tilde{x}^2} \left[\sigma\left(\tilde{x},\tilde{t}\right) + E\left(\tilde{x},\tilde{t}\right)\ f^I\left(\tilde{x},\tilde{t}\right)\ \varepsilon^{**}\left(\tilde{x},\tilde{t}\right) \right] = 0 \tag{3.43}$$

The approximate (averaged) boundary conditions at free edges ($y = \pm 1$) are

$$\int_{-1}^{1} \sigma \, d\tilde{x} = 0 \ \text{ and } \int_{-1}^{1} \sigma \, \tilde{x} d\tilde{x} = 0. \tag{3.44}$$

The latter condition is satisfied automatically as a result of the problem symmetry.

Solving Eq. (3.43) in conjunction with Eqs (3.44) and (3.41) leads to the following expression for the axial strain

$$\varepsilon \left(\tilde{x}, \tilde{t} \right) = \frac{1}{E \left(\tilde{x}, \tilde{t} \right)} \int_{0}^{1} \varepsilon^{**} \left(\tilde{x}, \tilde{t} \right) E \left(\tilde{x}, \tilde{t} \right) f^{I} \left(\tilde{x}, \tilde{t} \right) d\tilde{x} \tag{3.45}$$

The coupled self-consistent estimates of the effective moduli E, ν are given by Eqs (3.13) and (3.14). However, the computations performed in Budiansky and O'Connell, [19], clearly show that for practical purposes Eqs (3.13) and (3.14) can be linearized in ω as

$$E \approx E_0 \left(1 - \frac{16}{9} \omega \right) \tag{3.46}$$

$$\nu \approx \nu_0 \left(1 - \frac{16}{9} \omega \right) \tag{3.47}$$

Approximation (3.46) of the effective Young's modulus holds with a very good accuracy for all values of the effective Poisson's ratio ν in (3.13). Expression (3.47)) approximates the effective Poisson ratio ν for those elastic materials whose Poisson's ratio in undamaged state ν_0 is less than 0.3, e.g. for concrete.

The parameter $\beta(\omega)$ now becomes

$$\beta \left(\omega \right) = \frac{3 \left[1 - \nu_0 \left(1 - \frac{16}{9}\omega \right) \right]}{2\dfrac{E_0}{E_e} \left(1 - \frac{16}{9}\omega \right) \left(1 - 2\nu_e \right) + \left[1 + \nu_0 \left(1 - \frac{16}{9}\omega \right) \right]} \tag{3.48}$$

The damage parameter ω can now be computed combining Eqs (3.36) and (3.48). The resulting cubic algebraic equation in terms of ω is omitted here for the sake of brevity.

So far, the microcracking due to the sulfate attack was attributed solely to the stress concentrations near the expanding ettringite crystals. The stresses resulting from the beam-column action of the specimen can be detrimental as well. Simple comparison of measured macrostrains, [85], indicate that the number of expanding crystals N_a is relatively small. Consequently, the local stress fields in the vicinity of expanding crystals vastly exceed macrostresses σ. Thus, the damage attributed to the compressive stresses in regions bordered by external surfaces represents a second-order effect which will be neglected in computations. On the other hand, the tensile stresses acting on the inner core of the specimen are capable of activating the preexisting microcracks, always present in the bulk of concrete due to bleeding, shrinkage, etc. A wide spectrum of models for the tension-induced damage could be found in the available literature. However, in order to keep the present model tractable, elastic-perfectly brittle behavior will be assumed in tension. Incorporation of any model of tension-induced damage is only a matter of computational complexity.

In the pre-critical range ($\sigma < \sigma_{ut}$, $\varepsilon < \varepsilon_{ut}$), the axial expansion can be computed from formula (3.45) after solving the diffusion-reaction equation (3.9). Here, the following final formula is obtained

$$\varepsilon\left(\tilde{x}=0\right) = \frac{v_a\left(d-1\right)c_0}{3E\left(0,\tilde{t}\right)} \int_0^1 E\left(\tilde{x},\tilde{t}\right) \tilde{c}^R\left(\tilde{x},\tilde{t}\right) \beta\left(\tilde{x},\tilde{t}\right) d\tilde{x} \qquad (3.49)$$

In the post-critical range ($\varepsilon > \varepsilon_{ut}$), the elastic solution (3.49) ceases to be valid. The simplest approach to determine the expansion in that range would consist in assuming that the stresses vanish after the tensile stresses reach the critical value σ_{ut}, i.e. when the macrocracks appear. Therefore, the expansion of the specimen is equal to the volume average of the unconstrained expansions of the ettringite crystals in the heavily damaged matrix:

$$\varepsilon\left(\tilde{x}=0\right) = f^I \varepsilon^{**} = \tfrac{1}{3} c_F^R \left(d-1\right) v_a \qquad (3.50)$$

where c_F^R is the moles of sulfate per unit volume used to produce ettringite in the fractured zone s (Fig. 16). The total axial strain in the specimen (strain-controlled case) is obtained by superimposing Eqs (3.49) and (3.50). The appearance of macrocracks in the tensile zone changes the boundary condition (3.40)$_3$ as follows

$$\frac{\partial \tilde{c}}{\partial \tilde{x}} = 0 \quad \text{at} \quad \tilde{x} = \pm\left(1-\tilde{s}\right) \quad \text{for} \quad t > t_{cr} \qquad (3.51)$$
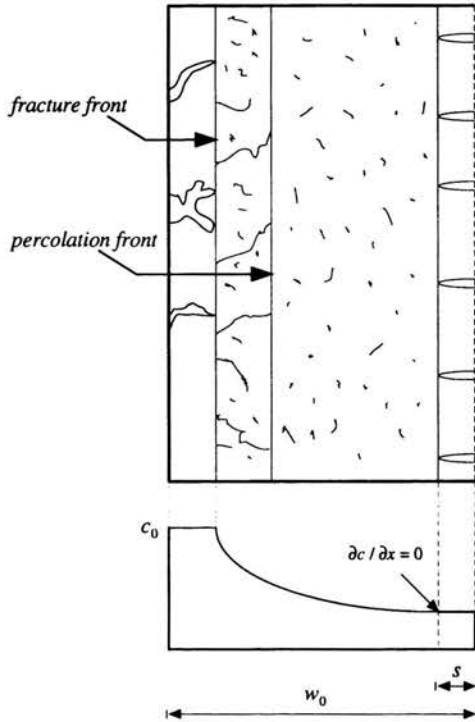
Figure 16: Schematic picture of damage evolution due to sulfate attack in mortar specimen

where $\tilde{s} = s/w_0$ (Fig. 16). With gradual increase in the microcrack density, the elastic modulus (3.46) decreases. At one point, the elastic modulus may vanish, i.e. the material becomes damaged to the extent that it loses its load-carrying capacity and disintegrates into separate fragments. The zone in which the material gets fragmented is contiguous to the external surface (Fig. 16). Such a behavior (spalling) is commonly observed in structural elements exposed to aggressive waters (e.g. [14]). Spalling is modeled by introducing a fracture front separating the heavily damaged (spalled) zone from the material which can still carry the loads. The fracture front is preceded by a percolation front, i.e. a surface behind which the microcracks form the first continuous paths. For the present analysis, the position of the percolation front will be identified with the plane in which $\omega_c = 0.182$, Eq. (3.15), while the fracture front (elastic percolation) is identified by $\omega_{ec}^{SC} = 9/16$, Eq. (3.46), when the secant elastic modulus vanishes. The emergence of the percolation

and/or the fracture front(s) has a dramatic impact on the effective diffusivity
(3.17). In particular, in the volume behind the fracture front it was assumed
that $D_{eff} \to \infty$ as ω approaches the critical value $9/16$. Consequently, the
concentration of sulfate in the zone swept by the fracture front has the
constant value $c = c_0$.

The following numerical values of the material parameters have been used
in the computations: $D_0 = 0.75 \cdot 10^{-12}\, m^2/s$ [14], accessible porosity of mortar
$\phi = 0.1$, porosity of ettringite $\phi_e = 0.18$ [90], $c_0 = 352\, mol/m^3$, initial
radius of C$_3$A particle $r_{a0} = 1\, \mu m$ [89], mass fraction of gypsum added to
Portland cement $f_g = 6\,\%$. The parameter d equals 9.96. Lacking precise
experimental data, reasonable values have been assigned to the remaining
parameters: Young's modulus of mortar $E_0 = 13\, GPa$, Young's modulus of
ettringite $E_e = E_0/5$, $\nu_0 = 0.3$, $\nu_e = 0.2$, ultimate compressive stress of
mortar $\sigma_{uc} = 40\, MPa$, fracture toughness of mortar $K_{Ic} = 0.2\, MN/m^{3/2}$.
The estimate of the rate constant k in the kinetic equation (3.8) is based on
the premise that no substantial degradation of mortar occurs in specimens
with C$_3$A content less than 5.5%. Therefore, the specimen with 4.3% C$_3$A in
[85] has been used for this purpose leading to $k = 1.35 \cdot 10^{-5}\, m^3/mol/s$.

The graph depicted in Fig. 17 represents the ability of the proposed
model to relate the macrostructural expansion to the chemical composition
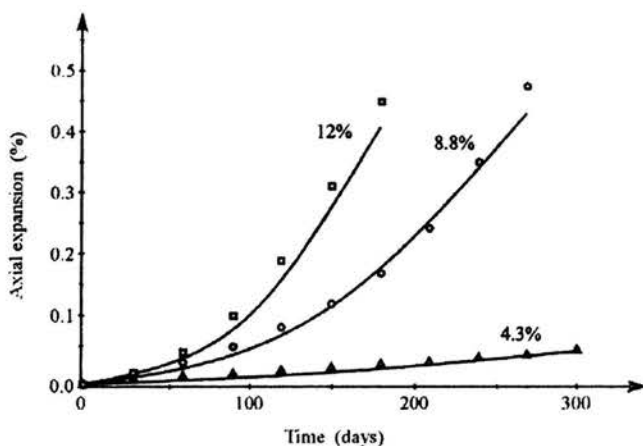of the mortar. The data of Ouyang et al., [85], are reproduced with

Figure 17: Axial expansion of mortar test bars due to external sulfate attack for different C$_3$A
contents vs. experimental data (symbols) of Ouyang et al., [85]

satisfactory accuracy. The model clearly distinguishes between mortars with a small concentration of C_3A and those rich in C_3A which disintegrate when subjected to water-borne sulfates for a prolonged time. The actual diffusion process in the experiment conducted by Ouyang et al., [85], is three-dimensional. Therefore, the 1D analysis carried out here for computational simplicity should be viewed as a lower bound for the expansions.

3.6. Summary and conclusions

The principal objective of the proposed model was to establish a direct relation between the chemical composition of the solid-ambient system and its response and/or durability. This objective has been reached by formulating an initial boundary value problem for the spatial and temporal degradation of a mortar prismatic bar exposed to external sulfate attack. The initial boundary-value problem couples unsteady diffusion, chemical reaction, and mechanical response. The coupling is both direct (i.e. sink term in the diffusion equation) and indirect through the transport properties (diffusivity and degrading stiffness). All material parameters, except for k, have been identified directly from the documented data. The rate constant of the chemical reaction k has been determined phenomenologically from the expansion of mortars with low concentration of C_3A. Once the parameter k had been determined by fitting the curve for the 4.3% concentration of C_3A, the formulated model has been able to predict the response for the other concentrations with remarkable ease and satisfactory accuracy.

One of the major advantages in micromechanical models is that they can readily be modified and extended to related problems. Various other chemical processes such as alkali-aggregate and cation exchange reactions, formation of calcium salts, carbonic acid attack, etc., causing degradation of concrete structures are just some of the examples that readily come to mind. Similarly, humidity, frost, and corrosion actions on metals belong to the same group of environment-assisted damage processes. In each particular case, the modeling strategy will be similar even though the details will change according to the dominant mechanism of microstructural changes.

4. Lattice modeling of brittle damage

Quite independently of the continuum mechanics community, brittle damage-fracture processes have also been investigated by statistical physicists who use an entirely different modeling methodology. Instead of analyzing stress fields at the crack tips (fracture mechanics) or introducing a priori a damage variable into a continuum constitutive description (damage mechanics), they simulate a continuous brittle matter by means of discrete (regular or random) lattices which are subjected to certain type of disorder. The essential feature of the representation of a solid by a discrete graph is that it provides an opportunity to model the inhomogeneity of the microstructure by assigning appropriate statistical properties to the lattice bonds. Two major types of disorder are usually distinguished in the relevant literature: quenched and annealed. The quenched disorder denotes an initial disorder introduced, for example, into the elastic constants or rupture thresholds of individual lattice elements, while the ensuing analysis of the system's fracture process is entirely deterministic. In the annealed disorder, the initial disorder may be absent but the analysis of the breaking process is stochastic.

Of several theoretical techniques available for dealing with highly disordered systems, the percolation model seems to be particularly appealing. The advantage of the percolation model consists in its almost game-like mathematical structure and a transparent description for spatially random processes. The percolation disorder is bi-modal in the sense that a defect either occupies the considered site (or bond) of the lattice with the probability p or is absent there with the probability $1-p$. As the bonds start to break under external tensile loading, the spatial patterns of defects (clusters) and their sequence of appearance are believed to mimic a real breaking process. The central questions posed in percolation and other statistical theories of disordered solids, are:

- What is the critical defect concentration p_c (*percolation threshold*) at which an infinite cluster appears spanning the opposite

sides of a lattice system?

- How would different processes and transport properties of a material behave in the vicinity of the percolation thresholds (*scaling laws*)?
- Is there any universal law that is common to all initial defect distributions?
- Does the maximum stress and the total number of ruptured bonds at overall failure follow any universal law?

A deeper insight into the lattice modeling of disordered systems can be gained by consulting the excellent monographs by Zallen, [116], Stauffer, [107], Herrmann and Roux, [42], Sahimi, [95].

4.1. Percolation model

This subsection will be focused only on those aspects of the percolation theory that may be of importance in modeling brittle damage and fracture. When examining the existing literature on the applications of percolation theory to brittle fracture and confronting it with the damage mechanics findings, several interesting observations can be made. For example, a crack density parameter identical to that of Budiansky-O'Connell (i.e. $\omega = N a^3 / V$) also appears in the percolation models. However, the way it was introduced is quite different and stems from purely geometrical considerations. It was shown by Scher and Zallen, [100], that the critical volume (area) fraction of spherical (or circular) non-overlapping voids at percolation is a *dimensional invariant* independent of the lattice type. To illustrate this statement, consider a simple case of circular voids whose centers are randomly located on the nodes of a regular, very large, two-dimensional lattice. The critical void area fraction f_c (critical porosity, critical lacunity) can be determined directly using the site percolation model as

$$f_c = v\, p_c^s, \qquad (4.1)$$

where p_c^s is the site percolation threshold, v is the filling (packing) factor for the considered lattice. The percolation threshold p_c^s denotes the critical fraction of lattice sites occupied by voids at the moment when an infinite void cluster transects a two-dimensional system. This situation corresponds to specimen's failure in the strain controlled test. Consequently, Eq. (4.1) can be rewritten as

$$f_c = (N A_{void})_c. \qquad (4.2)$$

According to Scher and Zallen, [100], the critical porosity f_c is a *universal constant* equal to 0.45 ± 0.03 irrespective of the lattice type, Table 1. This value persists to hold for all periodic two-dimensional lattices for which percolation data are available. A similar universality was also confirmed for the bond percolation model, [116] as shown by the last column in Table 1. As a consequence, this important result of Scher and Zallen implies that

1	2	3	4	5	6	7
Lattice type	Coordination number z	Percolation threshold (bond) p_c^b	Percolation threshold (bond) p_c^s	Filling factor ν	Critical porosity $\nu p_c^s = f_c$	Critical connectivity $z p_c^b$
Triangular (2D)	6	0.3473	0.500	0.9069	0.450	2.08
Square (2D)	4	0.5000	0.593	0.7854	0.470	2.00
Honeycomb (2D)	3	0.6257	0.698	0.6046	0.420	1.96
Face centered (3D)	12	0.1190	0.198	0.7405	0.147	1.43
Body centered (3D)	8	0.1790	0.245	0.6802	0.167	1.43
Cubic (3D)	6	0.247	0.311	0.5236	0.163	1.48

Table 1: Percolation thresholds and dimensional invariants for site and bond percolation on selected lattices. Filling factors given for non-overlapping circles (2D lattices) and spheres (3D lattices); after Zallen, [116].

the critical value of the Budiansky-O'Connell crack density parameter is a universal constant independent of the material microstructure. On the other hand, it should be emphasized that percolation thresholds p_c^s or p_c^b themselves are by no means dimensional invariants (see columns 3 and 4 in Table 1). The universality of f_c for lattices became afterwards a milestone for the development of the continuum percolation.

In the case of overlapping (intersecting, permeable, or soft-core) voids the problem belongs to the class of *continuum percolation* and becomes somewhat more complicated. It is first necessary to determine the probability of overlapping of the neighboring voids. The percolation threshold will then coincide with the appearance of an infinite cluster of overlapping voids whose centers need not to occupy nodes of a regular lattice. Obviously, two voids of equal radii r will overlap if the distance between their centers is smaller than $2r$. Shante and Kirkpatrick, [102], have shown that the probability that a randomly selected point does not belong to a circular void is equal to e^{-n}, where n is the mean number of circular voids within a distance r from that point. At percolation, the critical value of n becomes $n_c = z p_c^s/4$, where z

is the coordination (or connectivity) number denoting the number of closest nodes. The critical fractional area of voids in a 2D case is [2]:

$$f_c = 1 - e^{-B_c/4}, \tag{4.3}$$

where B_c is the average critical number of circle centers within a given circle (*mean number of object intersections*). In the 3D case, the critical fractional volume for permeable spherical voids becomes, [2]:

$$f_c = 1 - e^{-B_c/8}. \tag{4.4}$$

Similarly as the critical porosity (4.2) for hard-core voids, the critical values of B_c (hence f_c in Eqs (4.3) and (4.4)) manifest a universal behavior for soft-core voids. This universality was demonstrated by Pike and Seager, [88], in an extensive program of numerical simulations.

The geometrical interpretation of the universal parameter $\dot{B}_c$ is quite instructive. Balberg et al., [3], have found that

$$\begin{aligned} B_c &= N_c \langle A_{ex} \rangle \quad \text{(in two dimensions)}, \\ B_c &= N_c \langle V_{ex} \rangle \quad \text{(in three dimensions)} \end{aligned} \tag{4.5}$$

where N_c is the critical number of defects at percolation, and V_{ex} is the so-called excluded volume of an object, and $\langle V_{ex} \rangle$ is the proper average of the objects' excluded volumes.

The *excluded volume* V_{ex} (or excluded area A_{ex} in 2D) of an object (A) is enveloped by the locus of points formed by the centers of all surrounding, geometrically similar objects (B) which just touch the object (A) without intersecting it. In other words, if the center of an adjacent object (D) is within the excluded volume of a similar object (A), two objects will penetrate each other. For the circular voids of equal radii shown in Fig. 18 the excluded area is simply $A_{ex} = 4\pi r^2$. As pointed out by Balberg, [2], the advantage of this concept is that it accounts for the interaction between two objects. It associates a volume to objects which have no volume of their own (e.g. slits) and is simply related through Eq. (4.5) to the average number of bonds per site at percolation B_c, which is an invariant for a given object shape.

In the case of intersecting *slits*, the average number of intersections B_c is, indeed, a dimensional invariant but the critical crack density parameter $N_c r^2$ is not, [93]. As for uniformly distributed disks of constant radius r

and vanishing thickness (penny-shaped cracks), the critical crack density is $\omega_c = N_c\, r^3 = 0.182$, whereas the crack intersections density at percolation equals $B_c = N_c \langle V_{ex} \rangle = \pi^2 N_c\, r^3 = 1.80$, [20].
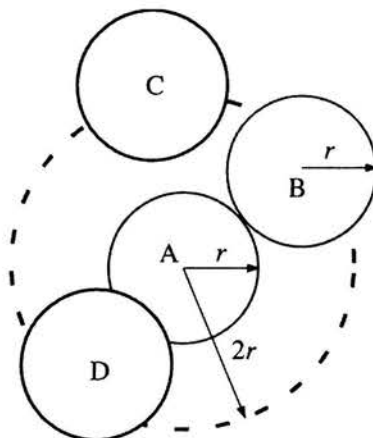

Figure 18: Geometrical concept of excluded area

The percolation studies confirm, at least for non-intersecting defects, the utility of the Budiansky-O'Connell crack density parameter in damage modeling. Although the starting points of the continuum and percolation models of brittle damage were quite different, both classes of models ended up with virtually the same parameter quantifying the evolving material deterioration. For non-intersecting defects, the critical value of this parameter has even been proven to be a dimensional invariant. Consequently, it may be concluded that for non-overlapping spherical or circular voids the strain-controlled rupture always happens at a constant value of the Budiansky-O'Connell damage parameter. A further conclusion is that Budiansky-O'Connell parameter is apparently proportional to the volume (area) fraction of defects, i.e. to the porosity. However, this interpretation may be misleading since the same damage parameter $\omega = N \langle r \rangle^2$ is also derived for slits, while $\omega = N \langle r \rangle^3$ for penny-shaped cracks, where any relation to material porosity is irrelevant, [5].

There is another aspect of the percolation theory that might be useful for the continuum mechanics descriptions of the effective properties of heterogeneous elastic solids. The mere fact that a spanning cluster emerges at a finite (critical) microdefect concentration furnishes kind of validity check

for the effective media/field methods at large microdefect concentrations. Consider, for instance, a dilution process of a plate made of perfectly elastic, isotropic and homogeneous material weakened by a large number of randomly distributed, non-overlapping, circular voids (plane stress case). Incidentally, this is a classical problem analyzed by the effective media/field models and the percolation theory alike. The expressions for the Young modulus estimated by the dilute distribution method (DD), the self-consistent method (SCM), and the differential scheme (DS) can be found almost in any book on micromechanics (e.g. [82]) and are given by

$$\frac{E^{DD}}{E_0} = \frac{1}{1+3f}, \quad \frac{E^{SCM}}{E_0} = 1 - 3f, \quad \frac{E^{DS}}{E_0} = (1-f)^3 \qquad (4.6)$$

where E_0 is the Young modulus of the undamaged material, $f = \sum_N (A_{void}/A) = \pi N \langle r^2 \rangle$ is the area fraction of voids, N being the number of voids per unit area. On the other hand, since this is a two-dimensional site percolation problem, the critical value of the void density is $f_c = (N A_{void})_c \approx 0.45$, Table 1. The variation of the elastic modulus vs. void fraction has also been investigated experimentally in Vavakin and Salganik, [114], Benguigui, [11, 12], Sieradzki and Li, [103], and others. The data provided by Benguigui, [11, 12], are best suited to check the accuracy of the expressions (4.6). The Benguigui's experiments were careful, force-controlled, elastic tension tests conducted on thin metallic sheets (Al, Cu) with non-overlapping holes punched randomly on the sites of a square lattice. The applied loading device allowed measurements very close to the percolation limit ($95\% p_c^s$). In Fig. 19, the theoretical estimations by the effective-medium methods (4.6) are depicted and confronted with the experimental results of Benguigui, [12]. Incidentally, Benguigui, [12] performed similar tests for circular holes allowed to overlap (continuum percolation). These tests confirmed with a very good accuracy that the critical area fraction of voids in 2D is, [102, 88, 2],

$$\phi_c = 1 - exp\left(1 - \langle A_{ex} \rangle /4\right) \approx 0.68. \qquad (4.7)$$

The scaling laws for the elastic modulus in the lattice (L) and continuum (C) percolation have the following forms

$$E \propto (f_c - f)^{T_L}, \quad E \propto (\phi_c - \phi)^{T_C}, \qquad (4.8)$$

where $(f_c - f)$ and $(\phi_c - \phi)$ are the lattice and continuum *proximity*

parameters, respectively. The measured values for T_L and T_C, [12, 13], fully agree with the theoretical numbers $T_L = 3.3 \pm 0.5$, $T_C = T_L + 3/2$, [37].

As remarked in Basista, [5], several interesting conclusions can be drawn when examining Fig. 19. For example, the Benguigui, [12], test data closely
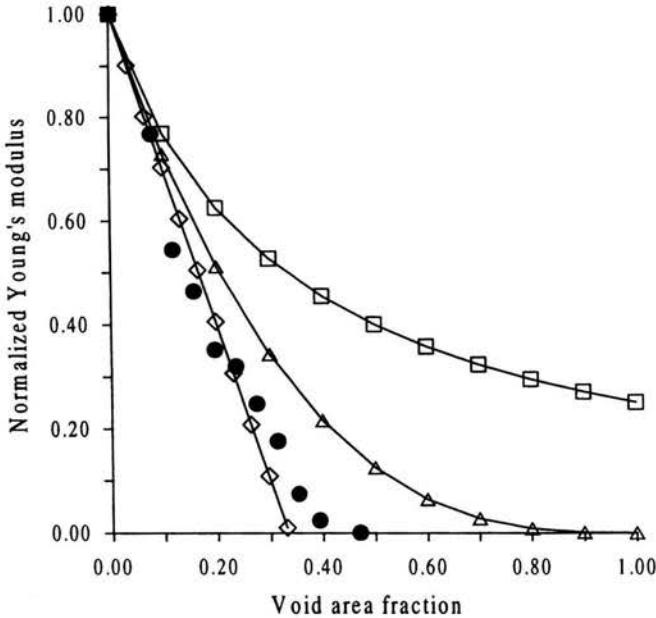

Figure 19: Effective elastic modulus E/E_0 for thin metal sheet with circular voids. Squares, triangles and diamonds represent DD, DS, and SCM predictions (4.6), respectively; data of Benguigui, [12], marked by circles

match the analytical result for the site percolation according to which the critical porosity on two-dimensional periodic lattices equals $f_c = 0.45 \pm 0.03$. As for the effective medium results, substantial differences have to be admitted even at small void densities. Moreover, only the self-consistent model predicts that the elastic modulus vanishes at a finite porosity $f_c^{SC} = 0.33$. This is consistent model predicts that the elastic modulus vanishes at finite porosity $f_c^{SC} = 0.33$ with the existence of the critical porosity $f_c^s = 0.45$, although f_c^{SC} clearly underestimates f_c^s. The dilute distribution model and the differential scheme do not recognize that the percolation threshold actually exists. The question arises here whether the density of randomly nucleating defects can be increased up to filling in the space. In

other words, can the existence of an RVE (thus volume averaging) be justified at very high defect concentrations? The answer offered by the percolation theory is that randomly nucleating defects will eventually self-organize and join the largest cluster making the specimen statistically non-homogeneous. This seems to set limits to the applicability of the effective medium/field theories provided that defects are not constrained in their random nucleation. Note that the effective continua models and the percolation models are applicable in different regimes and may thus be deemed complementary. The relatively unexplored region between those two, called the *crossover* regime, is currently under intensive studies by applied mechanicians as well as statistical physicists. In terms of continuum mechanics, the crossover regime corresponds to the softening portion of the stress-strain curve.

Despite unquestionable successes of the percolation theory in describing phenomena that approach the critical state, a certain amount of caution seems in order when using it to model brittle fracture processes. In a static case, the percolation model is *not* a suitable model to represent the damage-fracture process of brittle solids. It is commonly known that microcracks in brittle solids start to grow from the preexisting flaws. The longest and most favorably oriented microcrack, i.e. the one located perpendicularly to the maximum tensile stress direction, is the first to grow when its elastic strain energy release rate reaches the critical value. This, however, does not have much in common with a simple bi-modal type of disorder of the percolation model. Also, the existing percolation models are almost exclusively confined to tensile loading conditions whereas for brittle solids the compressive stress states are of primary importance.

On the other hand, the percolation model seems to be more suitable for nucleation-dominated fracture processes, e.g. dynamic fracture. Short duration times and high intensity of stress impulses amplify the random character of the microcrack nucleation and proliferation. In particular, brittle spall damage, which by its very nature involves random nucleation of defects under the action of tensile stress waves, offers a promising and yet unexplored field of possible applications of percolation theory. Some initial efforts in this direction can be found in [27] and [112].

4.2. Central-force lattices

Random nucleation processes are well captured by the percolation model. If, however, a damage process is dominated by the growth of microdefects (the case of brittle solids) more sophisticated types of disorder have to be employed when modeling the elastic rupture. For example, one could think of a continuous distribution function of the rupture strengths or stiffnesses of the lattice bonds. In statistical physics, these types of disorder are conveniently studied on regular lattice systems which are expected to mimic heterogeneous elastic continua. Typically, three main classes of lattices are distinguished:

- *fuse lattices* - electrical networks of random fuses (scalar equivalent of the vector problem of elastic rupture),
- *central-force lattices* (trusses) - elastic bonds (springs) that can freely rotate around their end points and carry axial forces only,
- *beam lattices* - elastic bonds carry axial forces, transverse forces, and bending moments.

In the recent past, an extensive research effort has been undertaken by the statistical physicists to investigate elastic rupture problem using fuse lattices (e.g. [25, 38]), central-force lattices ([10, 30, 39]), and beam lattices, [31, 42]. Limited by space, attention will here be focused on the central-force lattices.

More than a decade ago Hansen et al., [39], published an important study devoted to the rupture of central-force lattices. Inspired by that paper, Krajcinovic and Basista, [57], presented some links between the numerical simulations on central-force networks, and the analytical predictions of a simple parallel-bar model used in damage mechanics. Hansen et al., [39], considered a regular, 2D triangular lattice (Fig. 20a) consisting of nodes joined by elastic-brittle springs of identical elastic constants set to be unity. The quenched disorder was introduced in the bond rupture thresholds f_c. In Hansen et al., [39], the quenched disorder has the form of a uniform distribution of the rupture thresholds, Fig. 21a, which means that f_c can take any value between 0 and 1 with equal probability. The bottom and top rows of the lattice are attached to the rigid bars in order to assure uniformity of the applied displacement Λ. The boundary conditions in the horizontal direction are periodic, and the whole problem is treated within the limits of small deformations. Having introduced the quenched disorder in the bond rupture strengths, the forces in the bonds are computed using the conventional (deterministic) truss analysis. Four lattice sizes $L=4$, 8, 16,

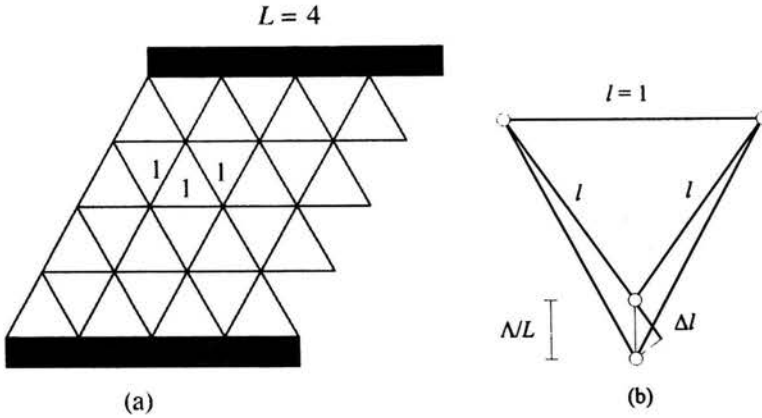24 were considered to ascertain the size effect.

Figure 20: (a) Central-force triangular lattice with rigid bars. (b) Estimation of strain in bond, [5]
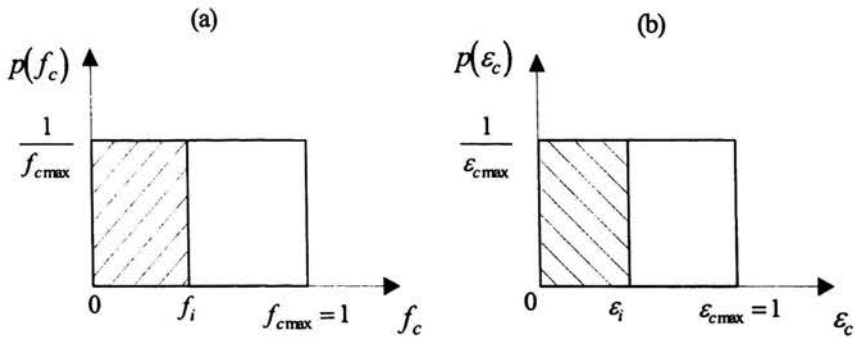

Figure 21: Probability density function for bond rupture thresholds: (a) in terms of forces (b) in terms of strains

If the force in a bond exceeded its rupture threshold, the bond was removed from the lattice, the forces in the extant bonds were recomputed and checked against the rupture criterion again, the next broken bond was then removed, and so on until the elastic modulus of the whole lattice dropped to zero. The computations were performed for each simulation (physical realization) which differed by the spatial distribution of bonds with different rupture strengths. Hansen et al., [39] generated 10000 4x4, 1000 8x8, 300

16x16, and 30 24x24 lattices over which the results were averaged. It is advisable to recall the basic symbols:

-L is the lattice size (number of rows),
-f_c is the bond rupture threshold,
-Λ, Λ_c is the total external displacement (subscript c indicates
            that "bond break was observed"),
-F, F_c is the total external force,
-f_j is the local force in a bond,
-N is the total number of diagonal (force carrying) bonds,
-n is the number of broken bonds,
-F_{max} is the maximum force recorded during a numerical simulation,
-n_{max} is the number of bonds broken at the maximum force,
-$\langle \cdot \rangle$ denotes an averaged quantity,
-K is the elastic modulus of the pristine lattice (set to 1 in, [39]).

In order to make the main results of Hansen et al., [39], traceable, the following *mean-field* analysis (not contained in the original paper) will now be performed. Consider a single lattice element, Fig. 20b and apply the external elongation Λ to the rigid bars. The strain in a stretched bond is given by

$$\varepsilon_i = \frac{\Delta l_i}{l_i} = \frac{\Lambda}{L}\frac{\sqrt{3}}{2},\tag{4.9}$$

where the bond length l is set to 1. Since the overall displacement is a stretch and the boundary conditions are periodic, only the diagonal bonds carry the forces thus are susceptible to rupture. It can be shown that the total number of diagonal bonds is $N = 2L^2$. Choosing the number of ruptured bonds n as the history-recording parameter, a physically appealing damage measure is the following scalar

$$D = \frac{n}{N} = \frac{n}{2L^2}.\tag{4.10}$$

On the other hand, the damage parameter (4.10) can be interpreted statistically as the cumulative probability function $P(f_i)$ of the assumed probability density function $p(f_c)$ for the bond rupture thresholds:

$$D = \int_0^{f_i} p(f_c)\,df_c = P(f_c < f_i),\tag{4.11}$$

where the rupture threshold of the weakest bond is 0. Damage is thus defined as the probability that the force in a bond f_i exceeds its rupture threshold

f_c. For the assumed uniform distribution of rupture thresholds (Fig. 21a) the damage parameter (4.11) takes the form (cf. [5])

$$D = \int_0^{f_i} \frac{1}{f_{max}} \, df_c = \frac{f_i}{f_{max}} = f_i, \text{ or } D = \int_0^{\varepsilon_i} \frac{1}{\varepsilon_{max}} \, d\varepsilon_c = \frac{\varepsilon_i}{\varepsilon_{max}} = \varepsilon_i, \quad (4.12)$$

where the latter of these formulas is expressed in terms of strains (cf. Fig. 21b). Comparing the two definitions of D, i.e. $(4.12)_2$ and (4.10), we get

$$n = 2L^2 \varepsilon_i, \tag{4.13}$$

which is identical to the relation (4) in [39]. Moreover, when Eq. (4.13) is combined with Eq. (4.9), an important linear equation (3) of the original paper Hansen et al., [39], is recovered:

$$\Lambda(n) = \frac{1}{\sqrt{3}} \frac{n}{L}. \tag{4.14}$$

Finally, dividing both sides of Eq. (4.14) by L, a linear proportionality between the damage $D = n/(2L^2)$ and the overall strain $\varepsilon = \Lambda/L$ is revealed. Remarkably, this linear regime was clearly confirmed by the respective numerical simulations in [39].

The primary objective in [39], though, was to establish a universal (size-independent) relation between the overall (average) force $\langle F_c(n) \rangle$ and the total elongation $\langle \Lambda_c(n) \rangle$, with the number of broken bonds n being a control variable. As a first step, the data $\langle F_c \rangle$ vs. n up to the apex were fitted according to the following parabola, [39]:

$$\langle F_c(n) \rangle = \left(1 - \alpha \frac{n}{L^2}\right) \langle \Lambda_c(n) \rangle. \tag{4.15}$$

Equivalently, one can say that a linear correction $\left(1 - \alpha n/L^2\right)$ was sought to the lattice elastic modulus (set to be 1 by definition). The authors hoped to find a value for the parameter α that is constant for all lattice sizes. However, it turned out that the best fit of the form (4.15) was obtained for $\alpha = 1.0$, $\alpha = 1.25$, $\alpha = 1.5$, $\alpha = 1.65$ corresponding to $L = 4$, $L = 8$, $L = 16$, $L = 24$, respectively. In conclusion, the linear *Ansatz* (4.15) proved insufficient to capture the degradation of the elastic modulus without a scale

effect. Hence, a universal relation was sought in the space of different variables assuming the following functional dependence, [39]:

$$\langle F_c(n) \rangle = L^\beta \, \Phi \left(\langle \Lambda_c(n) \rangle \, L^{-\gamma} \right), \tag{4.16}$$

where β, γ are unknown exponents and Φ is a universal function independent of the lattice size. In other words, Φ may be considered a universal function if the force-displacement data obtained from the numerical simulations for different lattice sizes, can be collapsed on a single master curve plotted in the reduced variables $\left\{ \langle F_c(n) \rangle / L^\beta \right\}$ vs. $\left\{ \langle \Lambda_c(n) \rangle / L^\gamma \right\}$. The authors found out that for $\beta = \gamma = \frac{3}{4}$ the trial function (4.16) fitted the simulation data exceedingly well. The only exception was the smallest size ($L = 4$) for which the computations were disregarded as unreliable. The parabolic fit (4.15) when combined with the mean-field estimate (4.14) gives

$$F_c(\Lambda_c) = \left(1 - \frac{\alpha\sqrt{3}}{L} \Lambda_c \right) \Lambda_c, \tag{4.17}$$

where the averaging symbols have been omitted. The form of α is dictated by the rescaling relation (4.16) as

$$\alpha \propto L^{1-\beta}, \tag{4.18}$$

with $\beta = \frac{3}{4}$, [39]. In addition to the central-force model, similar rescaling was obtained for the fuse model, [25], and for the elastic beam model, [42]. Quite surprisingly, the value of $\beta = \frac{3}{4}$ seems to be universal for all three models. In the post-peak regime, statistical fluctuations were very strong, thus it was not possible to find a universal exponent for all $\{ F_c(n)/L^\beta \}$ vs $\{ \Lambda_c(n)/L^\beta \}$ curves. Hence, in that regime the overall behavior of the lattice systems was *multifractal*.

It has been noticed in, [57], that the proportionality (4.18) can actually be expressed in the following exact form

$$\alpha = \beta L^{1-\beta}, \tag{4.19}$$

where the proponality factor and the universal exponent coincide having the constant value of $\beta = \frac{3}{4}$. This simple observation has far-reaching consequences. Each scaling law in, [39], can now be expressed in a closed analytical form, Table 2.

Inserting the equality (4.19) in the assumed force-displacement relation (4.17) yields

$$F_c = K \left[1 - \tilde{D}\left(L, \Lambda_c \right) \right] \Lambda_c = \bar{K}\, \Lambda_c, \qquad (4.20)$$

where $\bar{K} = K \left(1 - \tilde{D} \right)$ is the effective elastic modulus. Note that the elastic modulus of an undiluted lattice (set to 1 by definition) is here purposely marked by K. This formal labeling is needed in the anticipated comparison

Hansen et al., [39]	Krajcinovic and Basista, [57]
$\Lambda_{c\,max} \propto L^\beta$	$\Lambda_{c\,max} = \frac{1}{2\beta\sqrt{3}} L^\beta$
$n_{c\,max} \propto L^{\beta+1}$	$n_{c\,max} = \frac{1}{2\beta} L^{\beta+1}$
$F_{c\,max} \propto L^\beta$	$F_{c\,max} = \frac{1}{2}\Lambda_{c\,max}$

Table 2: Closed-form expressions obtained in [57], for scaling laws in [39]

with the parallel bar model. The damage parameter emerging in Eq. (4.20) is linearly proportional to the displacement Λ_c (or strain, $\varepsilon = \Lambda_c/L$) and is a function of the lattice size, namely

$$\tilde{D}(L) = \sqrt{3}\,\beta\,\Lambda_c\,L^{-\beta} = \sqrt{3}\beta\varepsilon\,L^{1-\beta} = 2\beta\,D\,L^{1-\beta}. \qquad (4.21)$$

In contrast, the effective elastic modulus (secant stiffness) $\bar{K} = F_c/\Lambda_c$ is independent of the lattice size. The last of the equalities (4.21) shows how the rescaled damage parameter $\tilde{D}$ is related to the density of ruptured bonds D, (4.10). Except for the scale effect, both parameters manifest linear dependence on the overall displacement. The damage parameter $\tilde{D}$ can also be rewritten as a function of the externally applied force

$$\tilde{D}(L, F) = \tfrac{1}{2} - \tfrac{1}{2}\sqrt{1 - 4\sqrt{3}\,\beta\,L^{-\beta}\,\frac{F}{K}}. \qquad (4.22)$$

It follows from Eq. (4.22) that in the unstressed state $\tilde{D}(F = 0) = 0$, while at the apex $\tilde{D}_{max}(F_{c\,max}) = 1/2$.

The parameters computed from the above analytical expressions are arranged in Table 3. The corresponding numerical data read off from Fig. 6 in Hansen et al. (1989) are added in parentheses. As suggested in Hansen et al. (1989) the data for $L = 4$ is disregarded.

Recall now the simplest form of a disordered system, i.e. a *parallel bar model* (fiber bundle with global sharing rule), Fig. 22. The parallel bar

L	α	$n_{c\ max}$	$n_{c\ max}/N$	$\Lambda_{c\ max}$	$F_{c\ max}$	$\tilde{D}_{max}$
4	1.06 (1.00)	9 (-)	0.280	1.09 (-)	0.54 (-)	1/2 (0.500)
8	1.26 (1.25)	25 (26)	0.195	1.83 (1.91)	0.92 (0.94)	1/2 (0.521)
16	1.50 (1.50)	85 (81)	0.166	3.08 (3.00)	1.54 (1.56)	1/2 (0.487)
24	1.66 (1.65)	173 (178)	0.155	4.17 (4.13)	2.09 (2.15)	1/2 (0.495)

Table 3: Data from [39] (in parentheses) vs. analytical formulas of Krajcinovic and Basista, [57]

model has been known since the early work of Daniels, [23], and often used afterwards in damage mechanics, [55, 60, 61] and statistical physics, [87, 105], to describe failure processes. It is a bundle of N loose bars (links) of equal
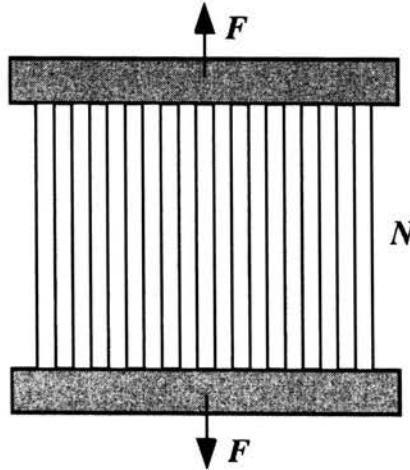

Figure 22: Parallel bar model

stiffness k carrying the external tensile load F. Since the links are loose there are tensile forces within the system but no shear forces. The rigid bars (buses) located at both ends of the system enforce equal elongation of all links. The initial stiffness of the whole system is $K = N k$. Each link is linear elastic and breaks when the tensile force in the link exceeds its rupture strength f_c. When a bond ruptures its force is released and has to be taken over (quasi-statically) by the remaining bonds. The distribution of link rupture strengths is prescribed in advance (quenched disorder) by the

probability density function $p(f_c)$. The position of a link in the bundle is inconsequential since all extant links equally participate in carrying the load (mean-field approximation). The parallel bar model rules out any spatial interactions. Also, the fiber bursting, [41], is not considered here. Hence, the macroresponse depends solely on the fraction of ruptured links (n/N). The scale effect is not accounted and, since there is no length parameter, the model is local. The process of damage and final rupture is attributed to the disorder in the rupture thresholds of material constituents. The model is not capable of accounting for the stress concentrations (hot spots). For such a system, the equilibrium of forces yields

$$F = (N - n)\, f = N \left(1 - \frac{n}{N}\right) \frac{K}{N} \Lambda = K\, (1 - D)\, \Lambda = \bar{K}\, \Lambda, \qquad (4.23)$$

where Λ is the elongation, while the force-displacement relation for an extant link is $f = k\,\Lambda = (K/N)\,\Lambda$; $D = (n/N)$ is the damage parameter (fraction of ruptured links) and $\bar{K}$ is the current secant effective elastic modulus of the system.

If the number of links is very large (rigorously speaking - infinite), the equilibrium equation (4.23) can be cast into an integral form as, [56]:

$$F = N \int\limits_{f}^{f_{max}} f\, p(f_c)\, df_c = k\Lambda \left[N \int\limits_{ku}^{f_{max}} p(f_c)\, df_c \right] = K\, (1 - D)\, \Lambda, \quad (4.24)$$

where the term in brackets represents the number of non-ruptured links. For the uniform strength distribution (Fig. 21), the force-displacement curve takes the form of a quadratic parabola, [60]:

$$F = K \left(1 - \frac{k\Lambda}{f_{cmax}}\right) \Lambda, \qquad (4.25)$$

where f_{cmax} is the rupture strength of the strongest link. The damage parameter $D = k\Lambda/f_{cmax}$ is linearly proportional to the elongation of the system. A similar dependence was observed for the central-force lattice, Eq. (4.14). It is easy to see that at the apex of the force-displacement parabola (4.25), it holds again

$$F_{cmax} = \tfrac{1}{2} K \Lambda_{cmax}. \qquad (4.26)$$

Comparing the last columns of Tables 3 and 2 with Eq. (4.26) it can be seen that for the same distributions of bond rupture thresholds the central-force lattice and the parallel bar system manifest *identical* response at the

apex, [57]. This is rather an unexpected result since the central-force lattice accounts for defect interactions whereas the parallel bar model totally ignores any defect interaction. Also, the size effect that is included in the central-force model disappears at the apex. In the parallel bar model the size effect is absent by definition.

4.3. Conclusions

Several important conclusions can now be formulated on the basis of the presented analysis.

1. The secant elastic modulus seems to be the proper choice for a damage parameter because:
   - all force-displacement simulation data in Hansen et al. (1989) can be collapsed on a single master curve irrespective of the lattice size,
   - at the apex it holds $\bar{K}_{cmax} = \frac{1}{2} K$ irrespective of the lattice size (4, 8, 16, 24),
   - at the apex it holds $\bar{K}_{cmax} = \frac{1}{2} K$ irrespective of the lattice type i.e. central-force lattice vs. parallel bar system; this conclusion needs to be checked for other network models.

2. The fraction of broken bonds (density of microcracks) is a poorer damage parameter as it manifests a size effect, cf. Eq. (4.21).

3. The lattice response under *tension* within the hardening regime is weakly affected by the defect interactions. The defect interactions, if present, should be profound at the apex and beyond it. The $(F_{cmax} - \Lambda_{cmax})$ equations that have been proved identical for the central-force lattice and parallel bar system at the apex indicate rather the opposite.

4. The mean-field assumption used in the analysis of the central-force lattice turned out to be correct. Consequently, it suffices to consider only the volume averages of microstructural disorder while higher statistical moments seem unnecessary when modeling the tensile lattice response.

References

1. AL-AMOUDI O.S.B., *Attack on plain and blended cement exposed to aggressive sulfate environments*, Cem. Concr. Comp., **24**, 305-316, 2002.

2. BALBERG I., *Recent developments in continuum percolation*, Phil. Mag., **B56**, 991-1003, 1987.

3. BALBERG I., ANDERSON C.H., ALEXANDER S. AND WAGNER N., *Excluded volume and its relation to the onset of percolation*, Phys. Rev. B, **30**, 3933-3943, 1984.

4. BARENBLATT G.I., ZHELTOV Iu.P. AND KOCHINA I.N., *Basic concepts in the theory of seepage of homogeneous liquids in fissured rocks*, Prikl. Mat. i Mekh., **24**,852-864, 1960.

5. BASISTA M., *Micromechanical and lattice modeling of brittle damage*, Habilitation thesis, Reports of Institute of Fundamental Technological Research, 3, Warszawa, 2001.

6. BASISTA M., *Micromechanics of Damage in Brittle Solids.*, in: Anisotropic Behaviour of Damaged Materials, J. Skrzypek and A.W. Ganczarski, Eds., Springer, Berlin, 221-258, 2003.

7. BASISTA M., GROSS D., *A note on brittle damage description*, Mech. Res. Comm., **16**, 147-154, 1989.

8. BASISTA M., GROSS D., *The sliding crack model of brittle deformation: an internal variable approach.*, Int. J. Solids Structures, **35**, 487-509, 1998.

9. BASISTA M. AND GROSS D., *A note on crack interactions in compression*, Int. J. Fracture, **102**, L67-L72, 2000.

10. BEALE P.D. AND SROLOVITZ D.J., *Elastic fracture in random materials*, Phys. Rev. B., **37**, 5500-5507, 1988.

11. BENGUIGUI L., *Experimental study of the elastic properties of a percolating system*, Phys. Rev. Lett., **53**, 2028-2030, 1984.

12. BENGUIGUI L., *Elasticity and fracture near a percolation threshold in two dimensions*, in: Fragmentation, Form and Flow in Fractured Media, R. Englman and Z. Jaeger, Eds., Annals Israel Phys. Soc., **8**, 288-293, 1986.

13. BENGUIGUI L., *Lattice and continuum percolation transport exponents: Experiments in two-dimensions*, Phys. Rev. B, **34**, 8176-8179,1986.

14. BICZOK I., *Concrete Corrosion Concrete Protection*, Akademia Kiado, Budapest, 1972.

15. Brace W.F., Bombolakis E.G., *A note on brittle crack growth in compression*, J. Geophys. Res., **68**, 3709-3713, 1963.

16. Brace W.F., Paulding B.W, Scholz C., *Dilatancy in the fracture of crystalline rocks*, J. Geophys. Res., **71**, 3939-3953, 1966.

17. Broek D., *Elementary Engineering Fracture Mechanics*, Noordhoff, Leyden, 1974.

18. Brown P., *Thaumasite formation and other forms of sulfate attack*, Cem. Concr. Comp., **24**, 301-303, 2002.

19. Budiansky B., O'Connell R.J., *Elastic moduli of cracked solid*, Int. J. Solids Structures, **12**, 81-97, 1976.

20. Charlaix E., *Percolation thresholds of a random array of discs: A numerical simulation*, J. Phys. A, **19**, L533-L536, 1986.

21. Christensen R.M., *A critical evaluation for a class of micro-mechanics models*, J. Mech. Phys. Solids, **38,** 379-404, 1990.

22. Costin L.S., *A microcrack model for the deformation and failure of brittle rock*, J. Geophys. Res., **88**, 9485-9492, 1983.

23. Daniels H.E., *The statistical theory of the strength of bundles of threads.*, Proc. Roy. Soc. London. A., **183**, 405-435, 1945.

24. Dawson B.E., *Kinetics and Mechanisms of Reactions*, Methuen Educational Ltd., London, 1973.

25. de Arcangelis L. and Herrmann H.J., *Scaling and multiscaling laws in random fuse networks*, Phys. Rev. B, **39**, 2678-2681, 1989.

26. Delaplace A., Pijaudier-Cabot G., Roux S., *Progressive damage in discrete models and consequences on continuum modelling*, J. Mech. Phys. Solids, **44,** 99-136, 1996.

27. Dienes J.K., *Permeability, percolation, and statistical crack mechanics, in: Issues on Rock Mechanics*, R.E. Goodman and F.E. Heuze, Eds., Proc. 23rd Symp. on Rock Mech., Berkeley, CA., 1982.

28. Dullien F.A.L., *Porous Media. Fluid Transport and Pore Structure*, Academic Press, New York, 1979.

29. Fanella D., Krajcinovic D., *A micromechanical model for concrete in compression*, Eng. Fract. Mech., **29**, 49-66, 1988.

30. Feng S. and Sen P.N., *Percolation on elastic networks: New exponents and threshold*, Phys. Rev. Lett., **52**, 216-280, 1984.

31. Feng S., Sen P.N., Halperin B.I. and Lobb C.J., *Percolation on two-dimensional elastic networks with rotationally invariant bond-bending forces*, Phys. Rev. B, **30**, 5386-5389, 1984.

32. Finlayson B.A., *Nonlinear Analysis in Chemical Engineering*, McGraw-Hill, New York, 1980.

33. GERMANOVICH L.N., CARTER B.J., INGRAFFEA A.R., DYSKIN A.V., LEE K.K., *Mechanics of 3-D crack growth under compressive loads,* In: Aubertin, Hassani, Mitri, Eds, Rock Mechanics. Balkema, Rotterdam, pp 1151-1160, 1996.

34. GROSS D., BECKER W., BASISTA M., *A simple mesostructural model for damage-induced inelasticity of brittle materials,* In: Boehler J-P, Ed., Yielding, Damage, and Failure of Anisotropic Solids. Mechanical Eng. Publ., London, pp 681-692, 1990.

35. GROSS D., *Spannungsintensitaetsfaktoren von Risssystemen,* Ing. Archiv, **51**, 301-310, 1982.

36. GUEGUEN Y. AND DIENES J., *Transport properties of rocks from statistics and percolation,* Math. Geol., **21**, 1-13, 1989.

37. HALPERIN B.I., FENG S. AND SEN P.N., *Differences between lattice and continuum percolation transport exponents,* Phys. Rev. Lett., **54**, 2391-2394, 1985.

38. HANSEN A., HINRICHSEN E.L. AND ROUX S., *Scale-invariant disorder in fracture and related breakdown phenomena,* Phys. Rev. B, **43**, 665-678, 1991.

39. HANSEN A., ROUX S. AND HERRMANN H.J., *Rupture of central-force lattices,* J. Physique, **50**, 733-744, 1989.

40. HANSEN W.C., *The chemistry of sulphate-resisting portland cement,* in: Performance of Concrete, E.G. Swenson, Ed., University of Toronto Press, 18-55, 1968.

41. HEMMER P.C. AND HANSEN A., *The distribution of simultaneous fiber failures in fiber bundles,* J. Appl. Mech., **59**, 909-914, 1992.

42. HERRMANN H.J., HANSEN A. AND ROUX S., *Fracture of disordered, elastic lattices in two dimensions,* Phys. Rev. B., **39**, 637-648, 1989.

43. HORII H, NEMAT-NASSER S., *Brittle failure in compression: splitting, faulting and brittle-ductile transition,* Phil. Trans. Roy Soc. London, **319**, 337-374, 1986.

44. HORII H. AND NEMAT-NASSER S., *Overall moduli of solids with microcracks: load induced anisotropy,* J. Mech. Phys. Solids, **31**, 155-171, 1983.

45. HORII H. AND NEMAT-NASSER S., *Compression-induced microcrack growth in brittle solids: axial splitting and shear failure,* J. Geophys. Res., **90**, 3105-3125, 1985.

46. INGRAFFEA A.R., *Theory of crack initiation and propagation in rock,* In: Atkinson B.K. ed Fracture Mechanics of Rock, Academic Press, London, 71-110, 1987.

47. JAEGER J.C., COOK N.G.W., *Fundamentals of Rock Mechanics,* Chapman and Hall, London, 1976.

48. JU J.W., *On two-dimensional self-consistent micromechanical damage models for brittle solids,* Int. J. Solids Structures, **27**, 227-258, 1991.

49. KACHANOV M., *Continuum model of medium with cracks,* J. Eng. Mech. Div ASCE, **106**, 1039-1051, 1980.

50. KACHANOV M., *A microcrack model of rock inelasticity. Part I: Frictional sliding on microcracks,* Mech. Mater., **1**, 19-27, 1982.

51. KACHANOV M., *Elastic solids with many cracks-a simple method of analysis*, Int. J. Solids Structures, **23**, 23-43, 1987.

52. KACHANOV M., *Elastic solids with many cracks and related problems*, In: Hutchinson J, Wu T eds Advances in Applied Mechanics, **30**, Academic Press New York, 259-445, 1993.

53. KEMENY J.M., COOK N.G.W., *Micromechanics of deformation in rocks*, In: Shah S.P., Ed., Toughening Mechanisms in Quasi-Brittle Materials, Kluwer, pp 155-188, 1991.

54. KENDALL K., *Complexities of compression failure*, Proc. R Soc. London, **A 361**, 245-263, 1978.

55. KRAJCINOVIC D., *Distributed damage theory of beams in pure bending*, J. Appl. Mech., **46**, 592-596, 1979.

56. KRAJCINOVIC D., *Damage Mechanics*, Elsevier, Amsterdam, 1996.

57. KRAJCINOVIC D., BASISTA M., *Rupture of central-force lattices revisited*, J. Physique I, **1**: 241-245, 1991.

58. KRAJCINOVIC D., FANELLA D., *A micromechanical damage model for concrete*, Eng. Fract. Mech. **25**, 585-596, 1986.

59. KRAJCINOVIC D., BASISTA M., MALLICK K. AND SUMARAC D., *Chemo-micromechanics of brittle solids*, J. Mech. Phys. Solids, **40**, 965-990, 1992.

60. KRAJCINOVIC D. AND SILVA M. A. G., *Statistical aspects of the continuous damage theory*, Int. J. Solids Structures **18**, 551-562, 1982.

61. KRAJCINOVIC D., LUBARDA V. AND SUMARAC D., *Fundamental aspects of brittle cooperative phenomena- Effective continua models*, Mech. Mater., **15**, 99-115, 1993.

62. LABUZ J.F., BRIDELL J.M., *Reducing frictional constraint in compression testing through lubrication*, Int. J. Rock Mech. Min. Sci. & Geomech. Abstr., **30**, 451-455, 1993.

63. LAUTERBACH B., *Zur mikrorissinduzierten Schädigung spröder Materialien*, Ph.D. thesis, Darmstadt University of Technology, 2001.

64. LAUTERBACH B. AND GROSS D., *Crack growth in brittle solids under compression*, Mech. Mater., **29**, 81-92, 1998.

65. LAWN B.R., MARSHALL D.B., *Nonlinear stress-strain curves for solids containing closed cracks with friction*, J. Mech. Phys. Solids, **46**, 85-113, 1998.

66. LAWN B.R, WILSHAW T.R., *Fracture of Brittle Solids*, Cambridge University Press, Cambridge, UK, 1975.

67. LEA F.M., *The Chemistry of Cement and Concrete*, Edward Arnold, London, 1970.

68. LEHNER F. AND KACHANOV M. *On modelling of "winged" cracks forming under compression*, Int. J. Fract., **77**, R69-R75, 1996.

69. LEMIEUX M.A., BRETTON P. AND TREMBLAY A.M.S. *Unified approach to numerical transfer matrix methods for disordered systems: Application to mixed crystals and to elasticity percolation*, J. Phys. Lett., **46**, L1-L7, 1985.

70. LOCKNER D., *The role of acoustic emission in the study of rock fracture,* Int. J. Rock Mech. Min. Sci. & Geomech. Abstr., **30**, 883-899, 1993.

71. LUBARDA V., KRAJCINOVIC D., *Damage tensors and the crack density distribution,* Int. J. Solids Structures 30: 2859-2877, 1993.

72. MAI Y.W., *Failure characterisation of fibre-reinforced cement composites with R-curve characteristics.*, In: Shah S.P., Ed., Toughening Mechanisms in Quasi-Brittle Materials, Kluwer Publ, The Netherlands, pp 489-527, 1991.

73. MAI Y.W., COTTERELL B., *Slow crack growth and fracture instability in cement composites,* Int. J. Cement Composites, **4**, 33-37, 1982.

74. MCHEDLOW-PETROSJAN O.P., *The Chemistry of Inorganic Structural Materials,* 2nd edition, Stroi-Izdat, Moscow, 1988.

75. MEHTA P.K., *Mechanism of sulphate attack on peortland cement concrete - another look,* Cem. Concr. Res., **13**, 401-406, 1983.

76. MEREDITH P.G., *Comparative fracture toughness testing of rocks,* In: Fracture Toughness and Fracture Energy Test Methods for Concrete and Rock Tohoku, Univ Sendai, Japan, pp 211-223, 1989.

77. MOSS W.C. AND GUPTA Y.M., *A constitutive model describing dilatancy and cracking in brittle rock,* J. Geophys. Res., **87**, 2985-2998, 1982.

78. MURA T., *Micromechanics of Defects in Solids,* Martinus Nijhoff Publ., The Hague, The Netherlands, 1987.

79. MURAKAMI Y., *Stress Intensity Factors Handbook,* Pergamon Press, New York, 1987.

80. MURAKAMI S. AND OHNO N., *A continuum theory of creep and creep damage,* In: Creep in Structures, A.R.S. Ponter and D.R. Hayhurst, Eds., 422-444, Springer Verlag, Berlin, 1981.

81. NEMAT-NASSER S. AND OBATA M., *A microcrack model of dilatancy in brittle materials,* J. Appl. Mech., **55**, 24-35, 1988.

82. NEMAT-NASSER S. AND HORI M., *Micromechanics: Overall Properties of Heterogeneous Materials,* Elsevier, Amsterdam, 1988.

83. OGAWA K. AND ROY D.M., C_4A_3S *hydration, ettringite formation, and its expansion mechanism: I. Expansion; ettringite stability,* Cem. Concr. Res., **11**, 741-750, 1981.

84. ORTIZ M., *A constitutive theory for the inelastic behavior of concrete,* Mech. Mater., **4**, 67-93, 1985.

85. OUYANG C., NANNI A., AND CHANG W.F., *Internal and external sources of sulphate ions in portland cement mortar: two types of chemical attack,* Cem. Concr. Res., **18**, 699-709, 1988.

86. PENG S. AND JOHNSON J.M., *Crack growth and faulting in cylindrical specimens of Chelmsford granite.* Int. J. Rock Mech. Min. Sci., **9**, 37-86, 1972.

87. PHOENIX S.L. AND TAYLOR H.M., *The asymptotic strength distribution of a general fibre bundle,* Adv. Appl. Prob., **5**, 200-216, 1973.

88. PIKE G.E. AND SEAGER C.H., *Percolation and conductivity: A computer study*, Phys. Rev. B, **10**, 1421-1446, 1974.

89. PLOWMAN C. AND CABRERA J.G., *Mechanism and kinetics of hydration of C_3A and C_4AF, extracted from cement*, Cem. Concr. Res., **14**, 238-248, 1984.

90. POMMERSHEIM J. AND CHANG J., *Kinetics of hydration of tricalcium aluminate in the presence of gypsum*, Cem. Concr. Res., **18**, 911-922, 1988.

91. RICE J.R., *Inelastic constitutive relations for solids: an internal-variable theory and its application to metal plasticity*, J. Mech. Phys. Solids, **19**, 433-455, 1971.

92. RICE J.R., *Continuum mechanics and thermodynamics of plasticity in relation to microscale deformation mechanisms*, in: Constitutive Equations in Plasticity, A.S. Argon, Ed., The MIT Press, Cambridge, MA, 23-79, 1975.

93. ROBINSON P.C., *Numerical calculations of critical densities for lines and planes*, J. Phys. A, **17**, 2823-2830, 1984.

94. RUDNICKI J.W. AND RICE J.R., *Conditions for the localization of deformation in pressure-sensitive dilatant materials*, J. Mech. Phys. Solids, **23**, 371-394, 1975.

95. SAHIMI M. *Applications of Percolation Theory*, Taylor & Francis Publ. London, UK., 1994.

96. SAHIMI M. AND GODDARD J.D., *Elastic percolation models for cohesive mechanical failure in heterogeneous systems*, Phys. Rev. B, **33**, 7848-7851, 1986.

97. SALGANIK R.L., *Transport processes in bodies with a large number of cracks*, Mech. Solids Inzhenerno-Fizicheskii Zhurnal, **27**, 1534-1538, 1974.

98. SAMMIS C.G. AND ASHBY M.F., *The failure of brittle porous solids under compressive stress states*, Acta Metall., **34**, 511-526, 1986.

99. SANTHANAM M., COHEN M.D., OLEK J., *Sulfate attack research - whither now?* Cem. Concr. Res., **31**, 845-851, 2001.

100. SCHER H. AND ZALLEN R., *Critical density in percolation processes*, J. Chem. Phys., **53**, 3759-3761, 1970.

101. SCHMIDT R.A. AND LUTZ T.J., *K_{Ic} and J_{Ic} of Westerly granite - effects of thickness and in-lane dimensions*, in Fracture Mechanics Applied to Brittle Materials, ASTM Spec. Techn. Publ. STP **678**, 166-182, 1979.

102. SHANTE V.K.S. AND KIRKPATRICK S., *An introduction to percolation theory*, Adv. Phys., **20**, 325-357, 1971.

103. SIERADZKI K. AND LI R., *Fracture behavior of a solid with random porosity*, Phys. Rev. Lett. **56**, 2509-2512, 1986.

104. SORNETTE D., *Critical transport and failure in continuum crack percolation*, J. Phys. France, **49**, 1365-1377, 1988.

105. SORNETTE D., *Elasticity and failure of a set of elements loaded in parallel*, J. Phys. A, **22**, L243-L250, 1989.

106. SOROKA I., *Portland Cement Paste and Concrete*, Chemical, New York, 1980.

107. STAUFFER D., *Introduction to Percolation Theory*, Taylor & Francis, London, UK., 1985.

108. STEINBRECH R.W., DICKERSON R.M. AND KLEIST G., *Characterisation of the fracture behavior of ceramics through analysis of crack propagation studies.*, in: Toughening Mechanisms in Quasi-Brittle Materials, S. P. Shah, Ed., Kluwer, 1991.

109. SUMARAC D., *Self-consistent model for the brittle response of solids.*, PhD Thesis, Civil Eng., Mechanics and Metallurgy Dept., University of Illinois at Chicago Circle, Chicago IL., 1987.

110. SWOBODA G. AND YANG Q., *An energy-based damage model of geomaterials - II. Deduction of damage evolution laws.*, Int. J. Solids Structures, **36**, 1735-1755, 1999.

111. TADA H., PARIS P., IRWIN G., *The Stress Analysis of Cracks Handbook.* Paris Productions Inc, St Louis, 1985.

112. TONKS D.L., *Disorder, percolation and wave propagation effects in ductile fracture,* in: High-Pressure Shock Compression of Solids II, L. Davison, D.E. Grady and M. Shahinpoor, Eds., Springer, 1996.

113. VAKULENKO A.A. AND KACHANOV M., *Continuum theory of cracked media,* Izv. AN SSSR, Mekh. Tverdogo Tela, **4**, 159-166, 1971.

114. VAVAKIN A.S. AND SALGANIK R.L., *Effective characteristics of nonhomogeneous media and with isolated nonhomogeneities,* Izv AN SSSR, Mekh. Tverdogo Tela, **10**, 65-75, 1975.

115. ZAITSEV, YU, *Inelastic properties of solids with random cracks,* in: Mechanics of Geomaterials, Z. Bazant, Ed., Wiley, 1985.

116. ZALLEN R., *The Physics of Amorphous Solids,* J. Wiley & Sons, New York, NY., 1983.

117. ZHANG A., WAGNER CH.F., AND DRESEN G. *Acoustic emission, microstructure, and damage model of dry and wet sandstone stressed to failure,* J. Geophys. Res., **101**, 17507-17524, 1996.

118. ZOBACK M.D., BYERLEE J.D., *The effect of cyclic differential stress on dilatancy in Westerly granite under uniaxial and triaxial conditions,* J. Geophys. Res., **80**, 1526-1530, 1975.

———◇———